

Sensorimotor experience remaps visual input to a heading-direction network

<https://doi.org/10.1038/s41586-019-1772-4>

Yvette E. Fisher¹, Jenny Lu¹, Isabel D'Alessandro¹ & Rachel I. Wilson^{1*}

Received: 28 December 2018

Accepted: 24 October 2019

Published online: 20 November 2019

In the *Drosophila* brain, ‘compass’ neurons track the orientation of the body and head (the fly’s heading) during navigation^{1,2}. In the absence of visual cues, the compass neuron network estimates heading by integrating self-movement signals over time^{3,4}. When a visual cue is present, the estimate of the network is more accurate^{1,3}. Visual inputs to compass neurons are thought to originate from inhibitory neurons called R neurons (also known as ring neurons); the receptive fields of R neurons tile visual space⁵. The axon of each R neuron overlaps with the dendrites of every compass neuron⁶, raising the question of how visual cues are integrated into the compass. Here, using *in vivo* whole-cell recordings, we show that a visual cue can evoke synaptic inhibition in compass neurons and that R neurons mediate this inhibition. Each compass neuron is inhibited only by specific visual cue positions, indicating that many potential connections from R neurons onto compass neurons are actually weak or silent. We also show that the pattern of visually evoked inhibition can reorganize over minutes as the fly explores an altered virtual-reality environment. Using ensemble calcium imaging, we demonstrate that this reorganization causes persistent changes in the compass coordinate frame. Taken together, our data suggest a model in which correlated pre- and postsynaptic activity triggers associative long-term synaptic depression of visually evoked inhibition in compass neurons. Our findings provide evidence for the theoretical proposal that associative plasticity of sensory inputs, when combined with attractor dynamics, can reconcile self-movement information with changing external cues to generate a coherent sense of direction^{7–12}.

The compass neurons in the *Drosophila* brain exhibit some resemblance to the head-direction cells of the mammalian brain^{13–16}. Visual cues stabilize the tuning preferences of mammalian head-direction cells¹⁵, and when a visual cue is rotated to a new horizontal position, the preferences of all of the head-direction neurons rotate together^{14,16}. It has been proposed that the mammalian head-direction system represents a ring attractor—a network in which global dynamics exhibit multiple stable states that unfold in a repeated sequence in response to an input^{7,17,18}. However, we do not know how visual cues anchor the mammalian head-direction system at a mechanistic level. It has been suggested that Hebbian synaptic plasticity of visual inputs enforces the correct mapping between sensory cues and attractor network states⁷.

Similar to mammalian head-direction cells, *Drosophila* compass neurons (called E-PG neurons) have properties of a ring attractor². Indeed, the dendrites of E-PG neurons are arranged in a ring in the brain (Fig. 1a). At any point in time, there is one ‘bump’ of activity in the E-PG ensemble, which rotates as the fly turns¹. This network receives continuous input from brain regions that track the rotational velocity of the fly via optic flow signals, proprioceptive signals and/or motor efference signals^{3,4}. These rotational velocity inputs push the bump around the circle. Visual cues make the position of the bump more accurate and stable^{1,3}. We do not know whether visual inputs to E-PG

neurons are plastic: the offset between the E-PG bump and the visual world is different in different individuals and it can occasionally change unpredictably within an individual^{1,3}; however, network instability alone does not provide evidence for synaptic plasticity.

The anatomy of R neuron axons is another reason to suspect the existence of synaptic plasticity in this network. Each R neuron axon overlaps with the dendrites of every E-PG neuron (Fig. 1b). If all these R-to-E-PG connections were functionally equivalent, information about the position of a visual cue would be discarded. Instead, it seems more likely that the all-to-all matrix of R-to-E-PG anatomical connections (Fig. 1c) represents a set of potential functional connections that can be repatterned during spatial learning. We therefore set out to test two hypotheses—first, that individual E-PG neurons respond selectively to specific visual cue positions and, second, that changes in visual-heading associations can trigger systematic, time-locked changes in the pattern of E-PG visual inputs.

Our first challenge was to isolate the synaptic input to E-PG neurons that is related to visual cue position, separate from the synaptic input related to the rotational velocity of the fly. We reasoned that this should be possible if we flashed visual cues transiently at randomized positions, preventing the fly from behaviourally fixating the stimulus. We therefore performed *in vivo* whole-cell recordings from E-PG

*Department of Neurobiology, Harvard Medical School, Boston, MA, USA. *e-mail: rachel_wilson@hms.harvard.edu

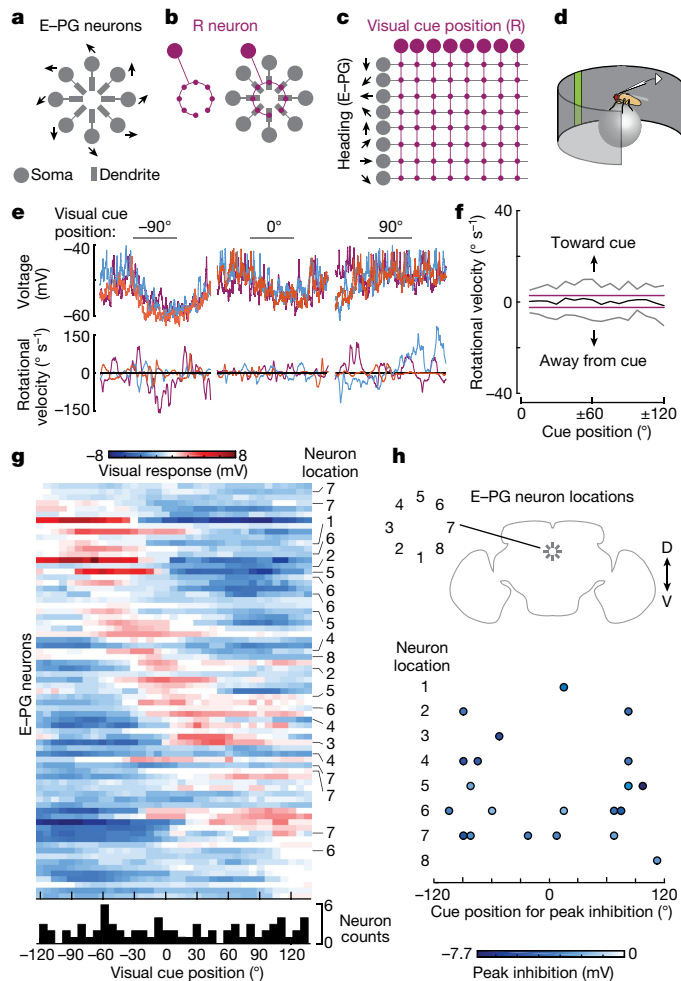


Fig. 1 | E-PG neurons are inhibited by visual cues at specific positions.

a, E-PG neuron dendrites form a circular array, with adjacent cells representing adjacent headings. **b**, The axon of each R neuron forms a ring (left) that overlaps all E-PG dendrites (right). Magenta boutons represent presynaptic terminals. **c**, An unwrapped R-to-E-PG matrix. The receptive fields of R neurons tile visual space. **d**, An E-PG neuron is recorded in whole-cell mode while the fly walks on a ball, surrounded by a panorama in which a cue flashes at random horizontal positions. **e**, Top, three example E-PG responses per cue position, for three different positions, all from the same recording. Bottom, the rotational velocity of the same fly (+ indicates right; - indicates left). Note that the fly behaves differently on different trials, but the neural response is essentially the same regardless of the fly's behaviour. Cue flash is 500 ms. **f**, Mean rotational velocity around cue presentation (black), \pm 1 s.d. (grey) across flies. Magenta lines show bootstrapped 95% confidence interval of the mean across flies after randomizing cue positions, Bonferroni-corrected; because the mean lies within these bounds, it is not significantly different from random. **g**, Summary of visual receptive fields of E-PG neurons (73 neurons in 68 flies). Cells are sorted by the cue position that evoked the most positive (least negative) response. Histogram shows the number of cells preferring each cue position. Some cells were filled to determine their location. **h**, Cue position eliciting peak inhibition versus neuron location (no significant correlation: circular correlation coefficient³⁶ = 0.097, P = 0.66, n = 21; see Extended Data Fig. 2g). D, dorsal; V, ventral.

neurons while flashing a bright vertical bar on a dark circular panorama at randomized horizontal positions (Fig. 1d). In a typical neuron, we observed hyperpolarization that was time-locked to flashes at specific positions (Fig. 1e). To verify that these neural responses are not related to the rotational velocity of the fly, we analysed the movement of the air-cushioned ball that the fly was standing on (Extended Data Fig. 1). Neural responses were unrelated to the rotational velocity of the flies

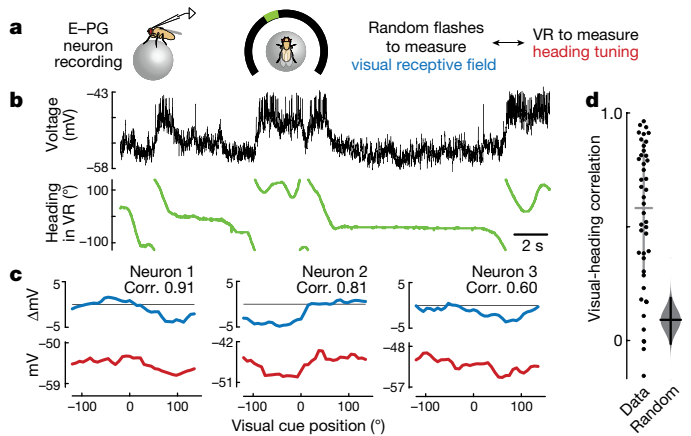


Fig. 2 | Visual receptive fields of E-PG neurons align with heading tuning.

a, Interleaved blocks measuring visual receptive fields and heading tuning. **b**, Top, E-PG voltage during a VR epoch. Bottom, VR heading. A heading of 0° means the cue is in front of the fly. **c**, Comparison of visual receptive fields (blue) and heading tuning (red) from three example E-PG neurons (from three flies, with Pearson's correlation coefficients). **d**, Pearson's correlation coefficients from 40 cells in 39 flies (all cells from Fig. 1). The mean and 95% confidence interval are shown as horizontal and vertical lines, respectively. The means of the data are outside the 95% confidence interval of a bootstrap distribution (grey violin plot) computed on randomized visual-heading pairings.

around the time of the visual flash (Fig. 1e), and there was no correlation between the rotational velocity and the flash (Fig. 1f). Therefore, we can interpret visually locked responses as synaptic inputs related to visual cue position. We call this the visual receptive field of the cell. The finding of visually evoked hyperpolarization is consistent with the fact that R neurons release the inhibitory neurotransmitter γ -aminobutyric acid (GABA)^{19,20}.

In almost every E-PG neuron, we found that some visual cue positions elicited hyperpolarization while other positions elicited no hyperpolarization (Fig. 1e, g). This suggests that each E-PG neuron receives relatively strong input from some R neurons but weak or non-existent input from other R neurons. In approximately half of the E-PG neurons, we also found that some cue positions elicited depolarization (Fig. 1g). Depolarization may represent disinhibition: because there is ongoing mutual inhibition between E-PG neurons², a visual cue that inhibits one E-PG neuron will disinhibit other E-PG neurons.

We found that different E-PG neurons had distinct visual receptive fields (Fig. 1g). When we sorted cells by the position that elicited the most positive (least negative) response, we found a uniform mapping of cue positions onto E-PG neurons (Fig. 1g). However, cue-evoked hyperpolarization was more prominent for lateral cue positions (Extended Data Fig. 2); this spatial bias is probably inherited from R neurons, because the receptive fields of R neurons are similarly biased towards lateral positions⁵.

When we managed to record sequentially from two adjacent E-PG neurons in the same brain, we found that they had adjacent receptive fields, as expected (Extended Data Fig. 3). However, when we pooled data across brains, we found no systematic relationship between the location of the dendrites of the E-PG neuron and its receptive field (Fig. 1h). Therefore, the mapping from visual space to compass coordinates is different across individuals.

Next, we investigated how the visual receptive field of an E-PG neuron compares with its heading tuning. To measure heading tuning, we allowed the fly to walk in closed-loop virtual reality (VR) in which the horizontal position of the cue was locked to the virtual heading of the fly (Fig. 2a, b). We periodically paused VR to map the visual receptive

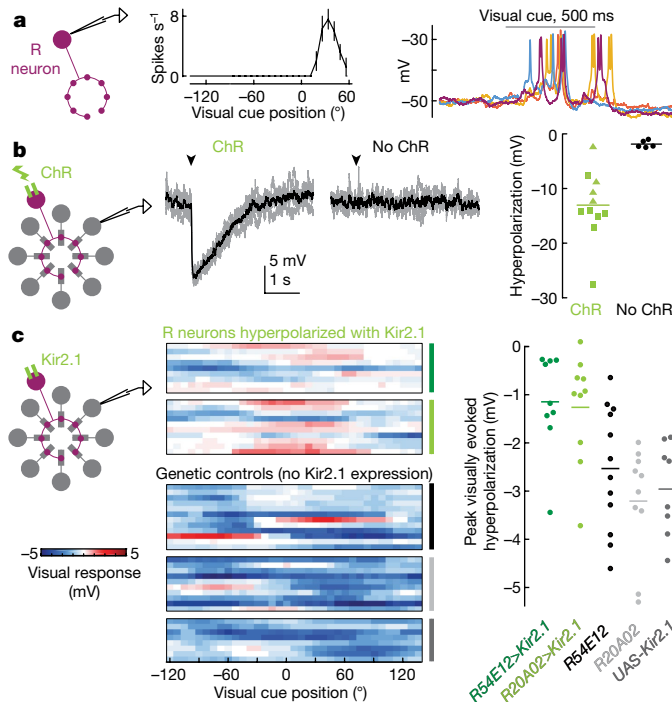
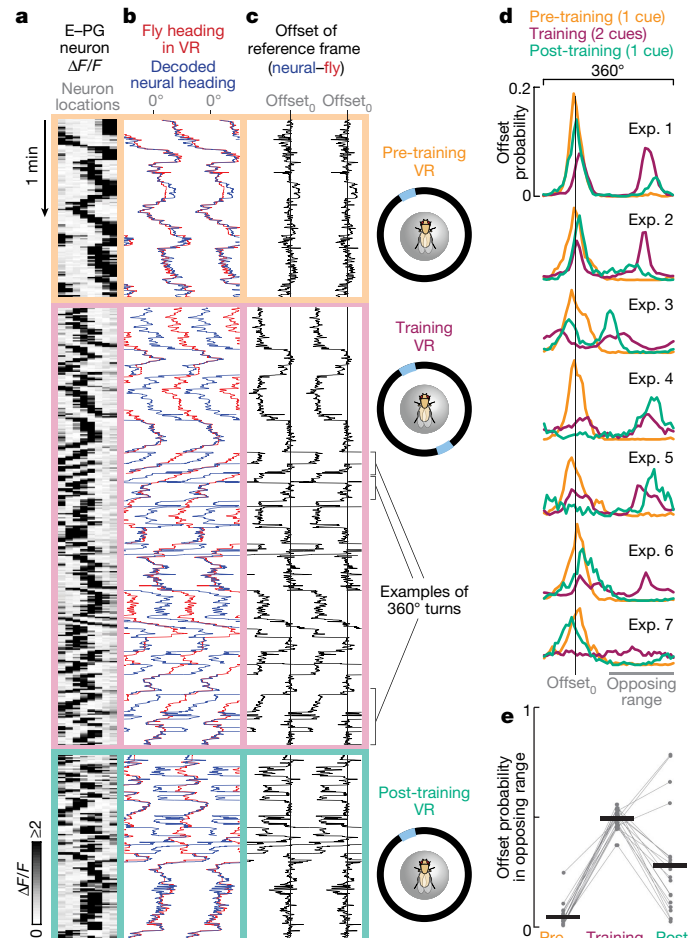


Fig. 3 | R neurons drive visually evoked inhibition in E-PG neurons. **a**, Left, visually evoked spike rates in an R neuron (mean \pm s.e.m. across trials, $n=5-6$ trials, R2 neurons). Right, four responses to repeated presentation of the best cue position for this neuron. We observed spatially tuned responses in 3 out of 7 R2 cells and 1 out of 3 R4d cells; an additional 3 R2 cells and 1 R4d cell responded to full-field illumination but were unresponsive to the cue or not spatially tuned. **b**, Left, responses of an E-PG neuron to optogenetic activation of R2 neurons via Chrimson (ChR), with four single trials in grey, mean in black. Middle, same as for the left panel, but with no Chrimson in R neurons, $n=4$ trials. Right, summary of mean evoked hyperpolarization with Chrimson in R neurons (squares, R2 neurons, $n=7$; triangles, R4d neurons, $n=4$) and controls ($n=5$). **c**, Left, E-PG visual receptive fields in flies in which R neurons were chronically hyperpolarized using Kir2.1 expression driven by *R54E12-Gal4* or *R20A02-Gal4* (green shades) versus controls (*R54E12-Gal4* only, *R20A02-Gal4* only, *UAS-Kir2.1* only, grey shades). Right, summary of peak visually evoked hyperpolarization, colour-coded as in the left panel (horizontal lines are means; $n=9, 10, 12, 10, 8$ cells, from left to right; *R54E12-Kir2.1* versus *R54E12/+* and *UAS/+*, $P=0.021$ and $P=0.0016$, respectively; *R20A02-Kir2.1* versus *R20A02/+* and *UAS/+*, $P=0.0046$ and $P=0.012$, respectively; two-sided Wilcoxon rank-sum tests).

field of the same neuron using brief random flashes. In most neurons, we found that the visual receptive field was correlated with heading tuning (Fig. 2c, d and Extended Data Figs. 3, 4). This result is notable because heading tuning reflects not only synaptic inputs related to visual cue position, but also synaptic inputs related to the rotational velocity of a fly. Imperfect alignment between these inputs may explain why some neurons showed poor correlations (Fig. 2d).

To confirm that R neurons are the actual source of visual responses in E-PG cells, we focused on two R neuron types (R2 and R4d) that respond to sparse visual cues⁵. First, we used whole-cell recordings to confirm that these R neuron types can be excited by the visual cue (Fig. 3a). Second, we verified that optogenetically activating either R2 or R4d neurons inhibits E-PG neurons (Fig. 3b). Third, we established that R neurons are required for normal visually evoked hyperpolarization in E-PG neurons. We used two independent driver lines to hyperpolarize R2 or R4d neurons by overexpressing the potassium channel Kir2.1 (Extended Data Fig. 5), and we confirmed that visually evoked hyperpolarization was attenuated (Fig. 3c and Extended Data Fig. 6) in both



genotypes. A few E-PG neurons still showed some visual responses, probably because neither driver line achieved complete coverage of R2 and R4d neurons (Extended Data Figs. 5, 6).

Next, we turned to our second hypothesis—that changes in visual-heading associations can trigger systematic, time-locked changes in the visual receptive fields of E-PG neurons. After allowing the fly to navigate in VR with one visual cue (the pre-training block), we switched to VR with two cues positioned 180° apart (the training block). In the training block, a full turn and a half-turn will arrive at an identical view of

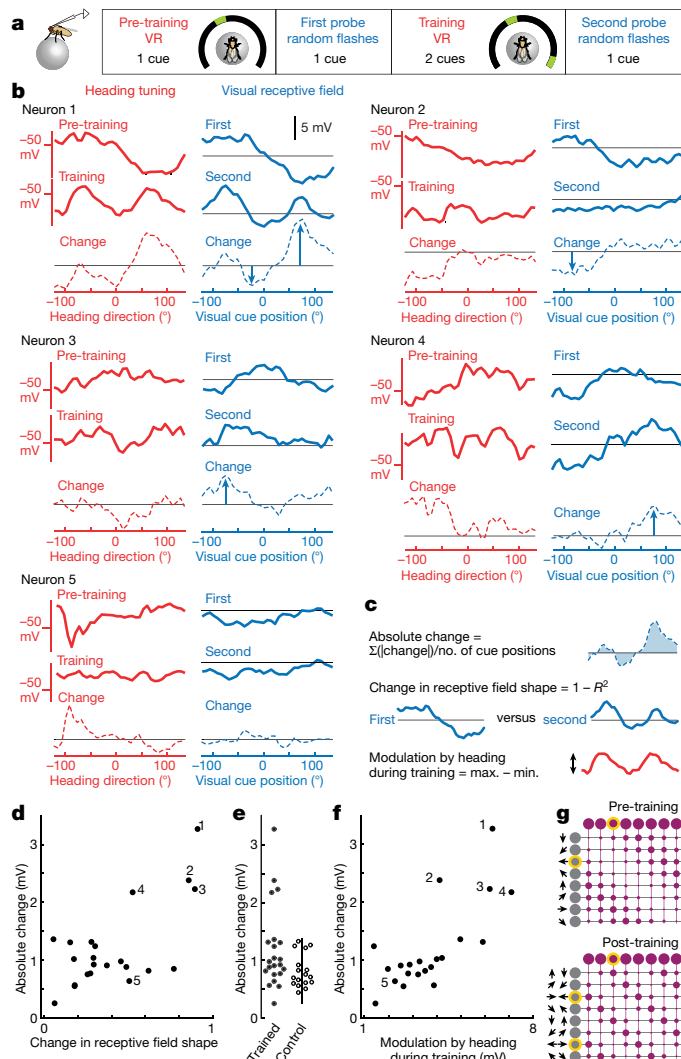


Fig. 5 | Visuomotor experience can remap visual input to E-PG neurons contingent on postsynaptic activity. **a**, After the fly navigated in VR with one cue (pre-training), we measured the visual receptive field of an E-PG neuron (first probe). Then the fly navigated in VR with two cues for 12 min (training) and we again measured the visual receptive field (second probe). **b**, Five example neurons. For each neuron, the red solid curve is heading tuning. Red dashed curve is the change in heading tuning (training minus pre-training). Blue solid curve is the visual receptive field. Blue dashed curve is the change in the visual receptive field (second probe minus first probe). Arrowheads mark large changes. Black vertical scale bar applies to all data in **b**. Thin black horizontal lines indicate zero change ($\Delta = 0 \text{ mV}$). Neuron 5 is an example with little modulation by heading during training and little change in visual receptive field. **c**, Explanation of metrics in **d-f**. **d**, Absolute change in visual receptive field, versus change in receptive field shape ($R^2 = 0.44, P = 0.000078$ testing t -statistic slope $\neq 0$; 22 E-PG neurons in 22 flies). **e**, Absolute change in visual receptive field post-training (22 E-PG neurons in 22 flies) versus controls (17 E-PG neurons in 17 flies). Post-training flies are significantly different from control flies ($P = 0.043$, two-sided Wilcoxon rank-sum test). Controls walked in a one-cue VR (not two-cue VR) between the first and second probe. Four training experiments had changes significantly larger than any controls ($>2 \text{ s.d.}$ above control mean, vertical bar); these are neurons 1–4. **f**, Absolute change in visual receptive field, versus modulation by heading during training ($R^2 = 0.52, P = 0.000016$ testing t -statistic slope $\neq 0$; 22 E-PG neurons in 22 flies). **g**, Schematic of model. When a visual cue appears, it activates specific R neurons (highlighted magenta cell) and this pushes the bump towards the E-PG neuron with minimal inhibition (highlighted grey cell). Training changes R-to-E-PG weights so that the bump toggles between two offsets during post-training. R neurons are ordered by receptive field position, and E-PG neurons are ordered by preferred heading direction (arrows).

the world, meaning the correlation between rotational velocity signals and visual cue position signals will be altered.

To assess the effect of training on network dynamics, we imaged calcium signals from the entire E-PG ensemble (Fig. 4a). During pre-training, there was a stable offset between the visual environment and the E-PG bump (Fig. 4b, c). During training, the offset toggled between two values approximately 180° apart. This result is expected, because there are two equally valid interpretations of the visual scene, yet only one bump can exist in the E-PG ensemble². When the fly made a 360° turn, we often saw the bump flow twice around 180° of the E-PG ensemble, skipping over the other 180° (Fig. 4a–c). Rotational velocity inputs to the E-PG network should drive the bump to traverse the full circle during a full turn^{3,4}; the skipping-over phenomenon thus indicates the dominance of visual position inputs over angular velocity inputs. The E-PG neurons that were traversed twice essentially displayed two preferred heading directions; this is reminiscent of the finding that some rat head-direction cells show two preferred directions in an environment with twofold rotational symmetry²¹.

Upon returning to a one-cue environment (post-training), the offset sometimes immediately settled into its original value. Often, however, this was not the case. Rather, the offset continued to toggle for several minutes, or else it immediately settled in a new value rather than the original one (Fig. 4d, e). Both of the latter two outcomes suggest a persistent, systematic change in the way that visual cues are mapped onto E-PG neurons. We observed one of the latter outcomes in about half of our experiments (Fig. 4e and Extended Data Fig. 7).

Finally, to investigate whether training changes visual receptive fields, we returned to E-PG whole-cell recordings (Fig. 5a). We began each experiment with one visual cue in VR (pre-training). We then switched to two visual cues in VR (training). Between each block of VR, we periodically paused to map the receptive field of the neuron using brief random flashes. Whereas we used a 360° panorama during calcium imaging, the spatial constraints of electrophysiology required us to map the 360° environment onto a 270° panorama^{1,10}.

During the training block, we found that some E-PG neurons were strongly modulated by the fly's heading. In these neurons, training produced changes in the visual receptive field (Fig. 5b, neurons 1–4). These changes were bidirectional, suggesting that visually evoked inhibition was depressed for some cue locations and potentiated for others. We quantified these changes by summing the absolute value of the change in the receptive field across all cue positions (absolute change; Fig. 5c). We also measured the change in the shape of the receptive field (Fig. 5c). These metrics were correlated across experiments (Fig. 5d); we never saw a large absolute change in the receptive field without a change in receptive field shape. We also never observed large changes in the receptive field under control conditions in which flies only experienced one cue in VR (but not two cues) during the period between the receptive field mapping epochs (Fig. 5e, Extended Data Figs. 8, 9).

By contrast, other E-PG neurons were essentially unmodulated by the fly's heading during training (Fig. 5b, neuron 5). These neurons may reside in sectors of the ensemble that were skipped over by the bump during training. Notably, training had almost no effect on visual receptive fields in these neurons (Fig. 5b and Extended Data Fig. 8). Overall, the magnitude of heading modulation during training was significantly correlated with the subsequent change in the visual receptive field (Fig. 5f). This correlation indicates that remapping depends on the activity of the E-PG neuron. Simply exposing the fly to the altered visual environment is not sufficient; rather, visual cues must intersect with heading representations in E-PG neurons. Because R-to-E-PG synapses are the site of intersection between visual responses and heading representations, they are the most likely locus of plasticity. In a companion study, Kim et al.²² used optogenetic manipulations to reach the same conclusion. Because R-neuron dendrites form a retinotopic map that is fairly consistent across flies⁵, it seems unlikely that the visual map in R-neuron dendrites is experience-dependent, further supporting the notion that R-to-E-PG synapses are the locus of plasticity.

Discussion

We propose that correlated pre- and postsynaptic activity triggers associative long-term synaptic depression of R-to-E-PG inhibition. This learning rule would explain why visual receptive fields and heading tuning are typically aligned in E-PG neurons. When an individual R neuron is activated by a visual cue, it should push the bump of activity towards the E-PG neurons that it inhibits most weakly (Fig. 5g). If the full ring attractor network agrees with this outcome, then long-term synaptic depression will occur and those weak R-to-E-PG synapses will become even weaker, further reinforcing this outcome. To ensure network stability, long-term synaptic depression should be balanced by long-term potentiation at R-to-E-PG synapses; the co-existence of long-term synaptic depression and long-term potentiation would also explain why we found bidirectional changes in visual receptive fields after training (Fig. 5b). These learning rules should produce a doubled pattern of R-to-E-PG synaptic weights after training in a two-cue world (Fig. 5g), reflecting the twofold symmetry of visuomotor correlations.

The key result of this study—that visual inputs to E-PG neurons are plastic—supports theoretical models that describe how a network can progressively establish a spatial map of the world by incorporating information about consistent sensory cues during exploration^{7–12}. In robotics, this process is called simultaneous localization and mapping²³. Our results provide direct experimental evidence for this type of unsupervised learning at the level of synaptic potentials *in vivo*.

In a simultaneous localization and mapping framework, visual cues are often local, meaning that they can change in size and apparent angle as they are approached; by contrast, we chose to use visual cues that could not be approached, simplifying the relationship between heading and visual cues. This choice was motivated by the known receptive field properties of R2 or R4d neurons, which seem adapted to detect the position of the Sun (or Moon). Specifically, R2 or R4d neurons have large inhibitory surrounds, meaning that they only respond robustly to isolated visual objects^{5,24} such as the Sun. The Sun is an ideal compass cue because it is effectively at infinity²⁵.

We propose that plasticity at R-to-E-PG synapses allows the position of the Sun to be flexibly associated with other compass cues, such as the pattern of linearly polarized light in the sky²⁶, sky-wide chromatic and intensity gradients^{27,28}, and wind^{29,30}. In other insects, the E-PG network responds to multiple sorts of compass cues^{31,32}, and navigation behaviour can depend on arbitrary learned associations between compass cues^{33–35}. In a companion study, Kim et al.²² provide evidence in favour of the idea that plasticity could be used to learn a complex conjunction of visual objects; in the future, to test this idea, it will be interesting to see whether any complex scene can generate a progressively more-stable heading representation (offset) during training. It will also be important to extend the approach that we have taken here to simulate a more naturalistic virtual world, to study how multiple types of cues influence the behaviour of this network and the organism.

Online content

Any methods, additional references, Nature Research reporting summaries, source data, extended data, supplementary information, acknowledgements, peer review information; details of author contributions and competing interests; and statements of data and code availability are available at <https://doi.org/10.1038/s41586-019-1772-4>.

1. Seelig, J. D. & Jayaraman, V. Neural dynamics for landmark orientation and angular path integration. *Nature* **521**, 186–191 (2015).
2. Kim, S. S., Rouault, H., Druckmann, S. & Jayaraman, V. Ring attractor dynamics in the *Drosophila* central brain. *Science* **356**, 849–853 (2017).

3. Green, J. et al. A neural circuit architecture for angular integration in *Drosophila*. *Nature* **546**, 101–106 (2017).
4. Turner-Evans, D. et al. Angular velocity integration in a fly heading circuit. *eLife* **6**, e23496 (2017).
5. Seelig, J. D. & Jayaraman, V. Feature detection and orientation tuning in the *Drosophila* central complex. *Nature* **503**, 262–266 (2013).
6. Omoto, J. J. et al. Neuronal constituents and putative interactions within the *Drosophila* ellipsoid body neuropil. *Front. Neural Circuits* **12**, 103 (2018).
7. Skaggs, W. E., Knierim, J. J., Kudrimoti, H. S. & McNaughton, B. L. A model of the neural basis of the rat's sense of direction. *Adv. Neural Inf. Process. Syst.* **7**, 173–180 (1995).
8. Milford, M. J., Wyeth, G. F. & Prasser, D. RatSLAM: A hippocampal model for simultaneous localization and mapping. In *Proc. International Conference on Robotics and Automation* 403–408 (2004).
9. Mulas, M., Wanick, N. & Conradt, J. Hebbian plasticity realigns grid cell activity with external sensory cues in continuous attractor models. *Front. Comput. Neurosci.* **10**, 13 (2016).
10. Cope, A. J., Sabo, C., Vasilaki, E., Barron, A. B. & Marshall, J. A. A computational model of the integration of landmarks and motion in the insect central complex. *PLoS ONE* **12**, e0172325 (2017).
11. Keinath, A. T., Epstein, R. A. & Balasubramanian, V. Environmental deformations dynamically shift the grid cell spatial metric. *eLife* **7**, e38169 (2018).
12. Ocko, S. A., Hardcastle, K., Giocomo, L. M. & Ganguly, S. Emergent elasticity in the neural code for space. *Proc. Natl Acad. Sci. USA* **115**, E11798–E11806 (2018).
13. Taube, J. S., Müller, R. U. & Ranck, J. B. Jr. Head-direction cells recorded from the postsubiculum in freely moving rats. I. Description and quantitative analysis. *J. Neurosci.* **10**, 420–435 (1990).
14. Taube, J. S., Müller, R. U. & Ranck, J. B. Jr. Head-direction cells recorded from the postsubiculum in freely moving rats. II. Effects of environmental manipulations. *J. Neurosci.* **10**, 436–447 (1990).
15. Mizumori, S. J. & Williams, J. D. Directionally selective mnemonic properties of neurons in the lateral dorsal nucleus of the thalamus of rats. *J. Neurosci.* **13**, 4015–4028 (1993).
16. Knierim, J. J., Kudrimoti, H. S. & McNaughton, B. L. Place cells, head direction cells, and the learning of landmark stability. *J. Neurosci.* **15**, 1648–1659 (1995).
17. Zhang, K. Representation of spatial orientation by the intrinsic dynamics of the head-direction cell ensemble: a theory. *J. Neurosci.* **16**, 2112–2126 (1996).
18. Xie, X., Hahnloser, R. H. & Seung, H. S. Double-ring network model of the head-direction system. *Phys. Rev. E* **66**, 041902 (2002).
19. Hanesch, U., Fischbach, K. F. & Heisenberg, M. Neuronal architecture of the central complex in *Drosophila melanogaster*. *Cell Tissue Res.* **257**, 343–366 (1989).
20. Zhang, Z., Li, X., Guo, J., Li, Y. & Guo, A. Two clusters of GABAergic ellipsoid body neurons modulate olfactory labile memory in *Drosophila*. *J. Neurosci.* **33**, 5175–5181 (2013).
21. Jacob, P. Y. et al. An independent, landmark-dominated head-direction signal in dysgranular retrosplenial cortex. *Nat. Neurosci.* **20**, 173–175 (2017).
22. Kim, S. S., Hermundstad, A. M., Romani, S., Abbott, L. F. & Jayaraman, V. Generation of stable heading representations in diverse visual scenes. *Nature* <https://doi.org/10.1038/s41586-019-1772-4> (2019).
23. Cadena, C. et al. Past, present, and future of simultaneous localization and mapping: toward the robust-perception age. *IEEE Trans. Robot.* **32**, 1309–1332 (2016).
24. Sun, Y. et al. Neural signatures of dynamic stimulus selection in *Drosophila*. *Nat. Neurosci.* **20**, 1104–1113 (2017).
25. Wehner, R. Astronavigation in insects. *Annu. Rev. Entomol.* **29**, 277–298 (1984).
26. Wehner, R. & Müller, M. The significance of direct sunlight and polarized skylight in the ant's celestial system of navigation. *Proc. Natl Acad. Sci. USA* **103**, 12575–12579 (2006).
27. el Jundi, B., Smolka, J., Baird, E., Byrne, M. J. & Dacke, M. Diurnal dung beetles use the intensity gradient and the polarization pattern of the sky for orientation. *J. Exp. Biol.* **217**, 2422–2429 (2014).
28. el Jundi, B., Foster, J. J., Byrne, M. J., Baird, E. & Dacke, M. Spectral information as an orientation cue in dung beetles. *Biol. Lett.* **11**, 20150656 (2015).
29. Bell, W. J., Tobin, T. R. & Sorensen, K. A. Orientation responses of individual larder beetles, *Dermestes ater* (Coleoptera, Dermestidae), to directional shifts in wind stimuli. *J. Insect Behav.* **2**, 787–801 (1989).
30. Heinzel, H.-G. & Böhm, H. The wind-orientation of walking carrion beetles. *J. Comp. Physiol. A* **164**, 775–786 (1989).
31. el Jundi, B. et al. Neural coding underlying the cue preference for celestial orientation. *Proc. Natl Acad. Sci. USA* **112**, 11395–11400 (2015).
32. Pegel, U., Pfeiffer, K. & Homberg, U. Integration of celestial compass cues in the central complex of the locust brain. *J. Exp. Biol.* **221**, jeb171207 (2018).
33. Müller, M. & Wehner, R. Wind and sky as compass cues in desert ant navigation. *Naturwissenschaften* **94**, 589–594 (2007).
34. el Jundi, B. et al. A snapshot-based mechanism for celestial orientation. *Curr. Biol.* **26**, 1456–1462 (2016).
35. Dacke, M. et al. Multimodal cue integration in the dung beetle compass. *Proc. Natl Acad. Sci. USA* **116**, 14248–14253 (2019).
36. Jammalamadaka, S. R. & SenGupta, A. *Topics in Circular Statistics* (World Scientific, 2001).

Publisher's note Springer Nature remains neutral with regard to jurisdictional claims in published maps and institutional affiliations.

© The Author(s), under exclusive licence to Springer Nature Limited 2019

Article

Methods

Fly husbandry and genotypes

Unless otherwise stated, flies were raised on standard cornmeal-molasses food (New Brown 19L, Archon Scientific) in an incubator on a 12-h:12-h light:dark cycle at 25 °C with humidity between around 50 and 70%.

All experiments with visual stimuli used flies with at least one wild-type copy of the *white* gene, and most electrophysiology experiments used flies with two copies of the wild-type *white* gene (as described below).

The experimenter was not blind to genotype because we did not use genetic perturbations; the exception is Fig. 3c (Kir2.1 perturbation). For the dataset shown in Fig. 3c, the experimenter was blind to genotype after the pilot phase for driver line *R20A02-Gal4*; because Fig. 3c pilot data were indistinguishable from subsequent data, all data were ultimately pooled; overall the experimenter was blind to genotype in 67% of these recordings. For the dataset obtained using the driver line *RS4E12-Gal4*, the experimenter was not blind to genotype because the experimental genotype was obtained at a lower-than-expected (sub-Mendelian) frequency, making it impractical to blind the experimenter.

Genotypes of fly stocks used in each figure are as follows. For Figs. 1, 2, 5 and Extended Data Figs. 1–4, 8, 9, we used *P{2OXUAS-IVS-mCD8::GFP}attP40/P{2OXUAS-IVS-mCD8::GFP}attP40; P{R60D05-Gal4}attP2/P{R60D05-Gal4}attP2* flies. For Fig. 3a, we used *P{2OXUAS-IVS-mCD8::GFP}attP40/P{2OXUAS-IVS-mCD8::GFP}attP40; P{GawB}EB1/+* flies. For Fig. 3b (R2 activation), we used *w/+; P{R19C08-lexA}attP40/P{2OXUAS-IVS-mCD8::GFP}attP40; PBac{13xLexAop2-IVS-Syn21-Chrimson::tdT-3.1}VK00005/P{R60D05-Gal4}attP2* flies. For Fig. 3b (R4d activation), we used *w/+; P{R60D05-lexA}attP40/P{13XLexAop2-mCD8::GFP}attP40; P{2OXUAS-CsChrimson-tdTomato}VK00005/P{R12B01-Gal4}attP2* flies. For Fig. 3b (no Chrimson), we used *P{2OXUAS-IVS-mCD8::GFP}attP40/P{2OXUAS-IVS-mCD8::GFP}attP40; P{R60D05-Gal4}attP2/P{R60D05-Gal4}attP2* flies. For Fig. 3c and Extended Data Fig. 6 (Kir2.1 silencing, driver 1), we used *+/w; P{R60D05-lexA}attP40/P{13XLexAop2-mCD8::GFP}attP40; P{R20A02-Gal4}attP2/P{UAS-Hsap|KCNJ2.eGFP}* flies. For Fig. 3c and Extended Data Fig. 6 (Kir2.1 silencing, driver 2), we used *+/w; P{R60D05-lexA}attP40/P{13XLexAop2-mCD8::GFP}attP40; P{RS4E12-Gal4}attP2/P{UAS-Hsap|KCNJ2.eGFP}* flies. For Fig. 3c and Extended Data Fig. 6 (UAS-only controls), we used *+/w; P{R60D05-lexA}attP40/P{13XLexAop2-mCD8::GFP}attP40; +/P{UAS-Hsap|KCNJ2.eGFP}* flies. For Fig. 3c and Extended Data Fig. 6 (Gal4-only controls), we used *+/w; P{GMR60D05-lexA}attP40/P{13XLexAop2-mCD8::GFP}attP40; +/P{R20A02-Gal4}attP2* flies and *+/w; P{GMR60D05-lexA}attP40/P{13XLexAop2-mCD8::GFP}attP40; +/P{RS4E12-Gal4}attP2* flies. For Fig. 4 and Extended Data Fig. 7, we used *+/w; P{UAS-GCaMP6f}attP40/+; P{R60D05-Gal4}attP2/+* flies. For Extended Data Fig. 5, we used *R57C10-FLPG5.PEST; UAS(FRT.stop)myr::smGdP-HA, UAS(FRT.stop)myr::smGdP-V5, UAS(FRT.stop)myr::smGdP-Flag/R20A02-Gal4, R57C10-FLPG5.PEST; UAS(FRT.stop)myr::smGdP-HA, UAS(FRT.stop)myr::smGdP-V5, UAS(FRT.stop)myr::smGdP-Flag/RS4E12-Gal4* flies.

Origins of transgenic stocks

The following GMR Gal4 lines were obtained from the Bloomington *Drosophila* Stock Center (BDSC) and were described previously³⁷: *P{R60D05-Gal4}attP2, P{R60D05-lexA}attP40, P{R19C08-lexA}attP40, P{R12B01-Gal4}attP2, P{RS4E12-Gal4}attP2, P{R20A02-Gal4}attP2*. The *P{GawB}EB1* line was also obtained from the BDSC and was described previously³⁸.

P{2OXUAS-IVS-mCD8::GFP}attP40 was a gift from B. Pfeiffer and G. Rubin and was described previously³⁹. *P{13XLexAop2-mCD8::GFP}attP40* was obtained from the BDSC and was described previously³⁹. *PBac{13xLexAop2-IVS-Syn21-Chrimson::tdT-3.1}VK00005* was a gift from B. Pfeiffer and D. Anderson and was described previously⁴⁰. *P{2OXUAS-CsChrimson-tdTomato}VK00005* was a gift from J. Tuthill who obtained

it from B. Pfeiffer. (Note that we have confirmed that this CsChrimson insert is on the third chromosome, but it may not be in *VK00005*, given the recombination frequencies observed in our laboratory. We have confirmed that this insertion does generate tdTomato expression and light-evoked currents in *Gal4⁺* cells.) *P{UAS-Hsap|KCNJ2.eGFP}7* was obtained from the BDSC and was described previously⁴¹. *P{UAS-GCamp6f}attP40* was obtained from the BDSC through T. Clandinin and was described previously⁴².

Transgenes for MultiColor FlpOut were obtained from the BDSC and were described previously⁴³, including *w[1118]P{y/+t7.7}w[+mC] = GMR57C10-FLPG5.PEST; su(Hw)attP8; PBac{y/+mDint2}* and *w[+mC] = 10xUAS(FRT.stop)myr::smGdP-HA; VK00005P{y/+t7.7}w[+mC] = 10xUAS(FRT.stop)myr::smGdP-V5-THS-10xUAS(FRT.stop)myr::smGdP-Flag; su(Hw)attP1*.

Fly preparation and dissection

Newly eclosed virgin female flies were anaesthetized on ice (electrophysiology) or CO₂ (imaging) and were collected around 3–10 h (electrophysiology) or 12–26 h (imaging) before the experiment. In some cases, to promote walking behaviour, we deprived the flies of food (but not water) for approximately 3–10 h before the experiment, and experiments were performed around the subjective evening of the fly (± 2 h from light to dark switch, Zeitgeber time 12); this was done in Fig. 5 and in 72% of recordings in Fig. 2. In all other experiments, there was no circadian restriction and flies were kept on food until the dissection. At the beginning of each dissection, the fly was cold-anaesthetized.

For electrophysiology experiments, the preparation holder consisted of flat titanium foil secured to an acrylic platform, with the foil oriented parallel to the horizontal body plane; the fly's head and body were gently pushed partway-through a hole in the foil. For E-PG neuron electrophysiology, the head was pitched forward so that the posterior surface was roughly parallel to the foil and most of each eye was under the foil. For R neuron electrophysiology, the head was positioned in a more upright angle, and a 90° bend was made in the foil to maximize the area of the eyes that was under the foil. For imaging experiments, the preparation holder was shaped like an inverted pyramid and was CNC machined from black acrylic (Autotiv), and the head was pitched forward so that the posterior surface was oriented dorsally and most of the eye was under the holder. The fly was always secured in the holder with epoxy (Loctite AA 3972) and cured using a brief (<1-s) pulse of ultraviolet light (LED-200, Electro-Lite Co). Wings were sometimes repositioned or removed. After the dorsal head was covered in saline, a hole was cut in the head capsule and some trachea were removed to expose the brain area of interest. To reduce brain movement, muscle 16 was removed, the proboscis was removed (Figs. 1–3, 5) or glued (Fig. 4) and the oesophagus was clipped or removed (Fig. 4). For electrophysiology, an aperture was made in the perineural sheath around the somata of interest either by ripping gently with fine forceps or by using suction from a patch pipette filled with external solution.

The external solution contained (in mM): 103 NaCl, 3 KCl, 5 N-tris(hydroxymethyl) methyl-2-aminoethane-sulfonic acid, 8 trehalose, 10 glucose, 26 NaHCO₃, 1 NaH₂PO₄, 1.5 CaCl₂ and 4 MgCl₂, with osmolarity adjusted to 270–273 mOsm. External solution was bubbled with 95% O₂ and 5% CO₂ and reached a final pH of 7.3. External solution was continuously perfused over the brain during electrophysiology and before imaging.

Patch-clamp recordings

Patch pipettes were made from borosilicate glass (Sutter, 1.5 mm o.d., 86 mm i.d.) using a Sutter P-97 puller. For E-PG recordings, the pipette was fire-polished after pulling⁴⁴ using a microforge (ALA Scientific Instruments) to achieve a final resistance of 8–15 MΩ. For R neuron recordings, pipettes (4–10 MΩ) were not fire-polished. The internal solution contained (in mM): 140 potassium aspartate, 10 4-(2-hydroxyethyl)-1-piperazineethanesulfonic acid, 4 MgATP,

0.5 Na₃GTP, 1 ethylene glycol tetraacetic acid, 1 KCl and 13 biocytin hydrazide. The pH was 7.3 and the osmolarity was adjusted to approximately 268 mOsm. To encourage walking, the external solution was heated before the experiment⁴⁵ to around 25–32 °C; this was done for all recordings in Fig. 5, 65% of recordings in Fig. 2 and 42% of recordings in Fig. 1. All other recordings were performed using external solution at room temperature.

To obtain patch-clamp recordings under visual control, we used an Olympus BX51WI microscope with a 40× water-immersion objective. Neurons were identified as GFP⁺ using a Hg-lamp source (U-LH100HG, Olympus) with an eGFP long-pass filter (U-N41012, Chroma). For experiments in which the fly was positioned on a foam ball, farred light was delivered from a fibre-coupled LED (740 nm, M740F2, Thorlabs) through a ferrule patch cable (200 μm core, Thorlabs) plugged into a fibre-optic cannula (1.25 mm SS ferrule 200 μm core, 0.22 NA, Thorlabs) glued to the recording platform, with the tip of the cannula around 1 cm behind the fly. In experiments without the ball, the brain was illuminated with 780 nm light via the microscope condenser, and after the recording was obtained, the condenser was lowered to prevent it from obscuring the fly's view of the visual panorama.

Recordings were obtained using an Axopatch 200B amplifier and a CV-203BU headstage (Molecular Devices). Voltage signals were low-pass filtered at 5 kHz before digitalization and then acquired with a NiDAQ PCI-6251 (National Instruments) at 20 kHz. Liquid junction-potential correction was performed post hoc by subtracting 13 mV from recorded voltages⁴⁶.

Two-photon calcium imaging

Imaging experiments were performed using a two-photon microscope with a moveable stage (Thorlabs Bergamo II) and a fast piezoelectric objective scanner (Physik Instrument P725) for volumetric imaging. For two-photon excitation, we used a Chameleon Vision-S Ti-Sapphire femtosecond laser tuned to 940 nm. Images were collected using a 20×/1.0 NA objective (Olympus). Emission fluorescence was filtered with a 525-nm bandpass filter (Thorlabs) and collected using a GaP photomultiplier tube (Hamamatsu).

The imaging region was centred on the protocerebral bridge, which is the brain region in which E-PG neuron axons terminate. For E-PG neurons, there is an orderly and stereotyped mapping from the location of the dendrite of the cell to the location of its axon terminal in the protocerebral bridge⁴⁷. Following previous studies^{3,4}, we chose to image E-PG axons rather than dendrites because the axons are more superficial, and so more optically accessible. The imaging region was 256 × 128 pixels, and 8–12 slices deep in the z axis (3–5 μm per slice), resulting in a 6–9 Hz volumetric scanning rate.

Volumetric z-scanning signals from the piezoelectric objective scanner were acquired simultaneously with analogue output signals from the visual panorama and analogue outputs from FicTrac via a NiDAQ PCI-6341 at 4 kHz. Two-photon calcium imaging data were acquired using ScanImage 2018 (Vidrio Technologies) with National Instruments hardware provided by Vidrio (NI PXIe-6341).

Measurement of locomotion

In all experiments except those shown in Fig. 3a, b, the fly stood on a 9-mm ball made of white foam (FR-4615, General Plastics) painted with black shapes. The ball floated above a plenum made of opaque ABS-like plastic (Figs. 1, 2, 3c, 5) or optically clear acrylic (Fig. 4) and was 3D-printed by Autotiv. Air was flowed into the plenum at the base and flowed out at the top in the semi-spherical depression that cradled the ball. The ball was illuminated by either an infrared LED (780 nm M780L3, Thorlabs) with a ground glass diffuser (DG10-220-MD, Thorlabs) (Figs. 1, 2, 3c, 5) or a round board 36 infrared LED lamp (SODIAL) (Fig. 4). The movement of the ball was tracked at approximately 60–70 Hz using a video camera (Firefly MV FMVU-03MTM, Point Grey) fitted with a Computar Macro zoom 0.3–1×, 1:4.5 lens (Figs. 1, 2, 3c, 5) or a Tamron

23FM08L 8-mm 1:1.4 lens (Fig. 4). In experiments in which we used a 360° visual panorama (Fig. 4), the image of the ball was reflected to the camera using a mirror (Thorlabs broadband dielectric mirror, 750–1,100 nm, BB1-E03) positioned below the ball. Machine vision software (FicTrac) converted the image of the ball to an estimate of the position of the ball in all three axes of rotation⁴⁸. FicTrac was modified to send real-time analogue measurements of all three motion axes of the ball to a USB DAQ (USB-3101, Measurement Computing). For closed-loop experiments, the yaw-position voltage signal was used to update the azimuthal position of the visual cues displayed on the panorama.

Visual panorama

Visual stimuli were presented using a circular panorama (IORodeo) composed of modular square panels⁴⁹. Each square panel was an 8 × 8 array of LEDs (8 × 8 'pixels') that refreshed at 372 Hz or faster⁴⁹. In electrophysiology experiments, these LEDs were green (peak = 525 nm). In imaging experiments, these LEDs were blue (peak = 470 nm) to minimize overlap with GCaMP6f emission. The vertical edge of the panorama was positioned approximately aligned with the vertical location of the fly. A single pixel along the top of the arena subtended around 3.6–3.7° of the visual field of the fly; this range of 0.1° is due to the fact that individual pixels within each flat 8 × 8 array have slightly different distances from the fly's eye. A single pixel at the bottom of the arena subtended around 2.7°. These differences in pixel size were not compensated for in our experiments.

In Figs. 1, 2, 3c, 5, we used a panorama composed of 9 × 2 panels. It spanned 270° azimuth and was oriented slightly asymmetrically so that it covered the azimuthal range from 127° left of the midline to 143° right of the midline. In Fig. 3a, we used a panorama composed of 6 × 2 panels that spanned 180° azimuth. In Fig. 4, we used a panorama composed of 12 × 2 panels that spanned 360° azimuth. All visual panoramas were the same height and spanned approximately 43° vertically within the visual field of the fly.

In electrophysiological experiments, to reduce electrical noise, the panorama was wrapped with a grounded copper mesh that was coloured with a black marker to reduce reflections. To further reduce reflections, the front surface of each panel was covered with a diffuser (SXF-0600 Snow White Light Diffuser, Decorative Films). In imaging experiments, instead of diffuser film, we used tracing paper as a diffuser, and four layers of filters (Rosco, R381, bandpass centre 440, full-width at half maximum of 40 nm) were used to minimize detection of the visual stimulus by the GCaMP6f emission collection channel.

Open- and closed-loop modes of visual stimuli

To map visual receptive fields, we used a bright vertical bar (2 pixels wide, 7°) that spanned the full height of the panorama (around 43°). The bar was flashed for 500 ms followed by 500 ms of darkness. During open-loop mode, the display updated at 50 Hz. The bar was presented in a pseudorandom order at 35 different evenly spaced azimuthal positions across the screen (−120° to 135°). During each open-loop epoch, each bar position was used 4–5 times in total. For R neuron recordings, fewer positions were used (27 positions, −139° to 56°) and each location was used 5–6 times in total.

To map heading tuning curves and to provide visuomotor training (closed-loop mode), we used a visual panorama containing either one vertical bar (one-cue) or two bars positioned on opposite sides of the virtual world (two-cue). Each vertical bar was identical to the bar we presented in open-loop mode. In closed-loop mode, we controlled the azimuthal position of the visual pattern using the yaw-position voltage output from FicTrac. Between consecutive closed-loop epochs were 3–40 s of darkness, after which we shifted the pattern randomly (Fig. 4) or by a variable 45° or 90° increment (Figs. 2, 5) before returning to closed loop. Analogue output signals from the visual panel system and from FicTrac were digitized with a NiDAQ PCI-6251 (National Instruments) at 20 kHz (electrophysiology) or with a NiDAQ PCI-6341

Article

(National Instruments) at 4 kHz (calcium imaging). In Fig. 4, the 360° yaw output signal was mapped directly to the 360° visual panorama. In Figs. 2, 5, we needed to use a 270° panorama owing to the space constraints imposed by the electrophysiology set-up; therefore, the 360° yaw output signal was mapped linearly to the 270° panorama so that objects did not disappear when they reached one edge of the panorama but instead moved immediately across the gap¹. Therefore, for example, whenever the fly made a 20° fictive right turn, the visual pattern would move 15° left. The exception to this is whenever the bar passed through the 90° gap; in that case, the bar traversed the gap immediately, as if the gap did not exist. How often this jump occurred varied from fly to fly depending on walking speed. We estimate that our most active flies experienced these 90° jumps of the cue around 10 times per minute during a typical one-cue closed-loop trial. Note that in the 270° panorama, the two-cue pattern contained two bars spaced 135° apart.

In pilot electrophysiology recordings, during closed-loop epochs, the 360° yaw output signal was mapped to 360° of visual space (rather than 270°). This meant that the visual cue was only displayed when it resided on the 270° panorama, and the cue simply disappeared when it moved into the 90° sector in which the panels were missing. The heading tuning data from these 16 recordings were not included in the final dataset, but some open-loop visual responses from these neurons are included in Fig. 1g. We did not observe any systematic differences in the open-loop visual responses of these neurons from pilot recordings.

Optogenetic stimulation

Chrimson⁵⁰-expressing flies were raised on cornmeal-agar medium supplemented with rehydrated potato flakes (Carolina Biological Supply) mixed with 100 µl of all-*trans*-retinal stock solution (Sigma; 17 mM in ethanol). Fly vials were wrapped in foil to prevent photo-conversion of the all-*trans*-retinal. Controls in Fig. 3b were raised on molasses food without all-*trans*-retinal. For optogenetic stimulation, we used the Hg-lamp source (U-LH100HG) to deliver a 5-ms pulse of green light (530–550 nm, 2–4 mW, TRITC–Cy3 filter cube, Chroma) through the objective. A shutter (Uniblitz Electronic) controlled the pulse duration.

Experimental epoch structure

Each open-loop epoch always lasted 150 s and consisted of a sequence of random cue flashes. Each closed-loop epoch lasted 4 min (Figs. 2, 5) or 2 min (Fig. 4), during which time the visual pattern was continuously present and rotated in proportion to the fly's fictive yaw velocity. In Fig. 1, open-loop epochs were usually interleaved with 4-min one-cue closed-loop epochs, although occasionally two open-loop epochs were delivered consecutively. In Fig. 2, at least one 4-min one-cue closed-loop epoch was presented before obtaining a recording, and after the recording was obtained, open-loop epochs and 4-min one-cue closed-loop epochs were interleaved. In Fig. 3c, only open-loop epochs were presented. In Fig. 4, for pre-training, we presented at least five 2-min one-cue closed-loop epochs. For training, we presented ten 2-min two-cue closed-loop epochs. For post-training, we presented at least two 2-min one-cue closed-loop epochs. In Figs. 5, 1–6 epochs of one-cue closed-loop experience were presented before obtaining an E-PG neuron recording. Once the recording was obtained, the epoch structure was as follows. First, for pre-training, we cycled through 4-min one-cue closed-loop epochs alternating with open-loop epochs, for a total of 2–6 cycles. For training, we presented three consecutive 4-min two-cue closed-loop epochs (experimental condition) or three consecutive 4-min one-cue closed-loop epochs (matched control condition). For post-training, we presented one open-loop epoch. This protocol was followed in all training experiments in Fig. 5, with two exceptions. In one case, pre-training consisted of an open-loop epoch, followed by a closed-loop epoch, followed by another open-loop epoch (that is, 1.5 cycles through the normal pre-training procedure). In the other case, during the closed-loop epochs before obtaining the recording, the fly

experienced a different visual pattern that consisted of sparse randomly distributed single pixels (a 'star field' pattern), and this fly also received two consecutive open-loop epochs (instead of one) during pre-training.

Immunohistochemistry

MultiColor FlpOut. In Extended Data Fig. 5, MultiColor FlpOut (MCFO) was used to identify the morphological types of R neurons labelled by *R20A02-Gal4*. MCFO immunostaining was performed essentially as described previously⁴³. Primary incubation solution contained mouse anti-Bruchpilot (1:30, Developmental Studies Hybridoma Bank, nc82), rat anti-Flag (1:200, Novus Biologicals), rabbit anti-haemagglutinin (HA; 1:300, Cell Signaling Technologies) antibodies and 5% normal goat serum (NGS) in PBST. Secondary incubation solution contained Alexa Fluor 488-conjugated goat anti-rabbit (1:250, Invitrogen), ATTO 647-conjugated goat anti-rat (1:400, Rockland) and Alexa Fluor 405-conjugated goat anti-mouse (1:500, Invitrogen) antibodies and 5% NGS in PBST. Tertiary incubation solution contained DyLight 550-conjugated mouse anti-V5 (1:500, Bio-Rad) antibody and 5% normal mouse serum in PBST.

Visualization of biocytin-filled neurons. Brains containing biocytin-filled neurons were processed after electrophysiological recording using standard procedures. Primary incubation solution contained mouse anti-Bruchpilot antibody (1:30, Developmental Studies Hybridoma Bank, nc82), chicken anti-GFP antibody (1:1,000, Abcam), Alexa Fluor 568-conjugated streptavidin (1:1,000, Invitrogen) and 5% NGS in PBST. Secondary incubation solution contained Alexa Fluor 488-conjugated goat anti-chicken antibody (1:250, Invitrogen), Alexa Fluor 633-conjugated goat anti-mouse antibody (1:250, Invitrogen), Alexa Fluor 568-conjugated streptavidin (1:1,000, Invitrogen) and 5% NGS in PBST.

Confocal microscopy and image analysis. Brains processed for MCFO were imaged using an Olympus FV1000 confocal microscope. Series of between 50 and 100 optical sections (1.0-µm spacing) were imaged using either a UPLFLN 40×/1.3 NA oil-immersion lens or a PLAPON 60×/1.42 NA oil-immersion lens. R neuron MCFO clones were classified into 11 subtypes according to previously published methods⁶ based on the consensus of two experts. Maximum intensity z-projections were rendered and adjusted using cropping and thresholding tools in Fiji (ImageJ) and assembled into figures using Illustrator (Adobe).

Confocal microscopy of brains processed for biocytin fills, or to assess expression of Kir2.1::eGFP within R neurons (Fig. 3), was performed using a Leica SP8 or Leica SPE equipped with a 40×/1.3 NA oil-immersion lens. Cell body counting of eGFP-labelled R neurons was performed independently by two experts using the Fiji Cell Counter plugin⁵¹, and the mean count for each brain hemisphere is reported (Extended Data Fig. 6).

Data analysis

Visual receptive fields of E-PG neurons. In Figs. 1g, 2c, 3c, and 5b (and Extended Data Figs. 1–4, 8, 9), visual responses were calculated by taking the mean voltage during the final 250 ms of the 500-ms cue flash, and subtracting the mean voltage during the 250 ms preceding the flash, averaged over all presentations of the cue at each position. For display, visual receptive field curves were often smoothed using a median filter with a width of three cue positions (Figs. 1g, 3c and Extended Data Fig. 2) or two cue positions (Figs. 2c, 5b and Extended Data Figs. 3, 4, 8, 9). Peak visually evoked hyperpolarization (Fig. 3c) and mean visually evoked hyperpolarization (Extended Data Fig. 6) were calculated on the median-filtered tuning curves.

Heading tuning of E-PG neurons. In Figs. 2, 5 (and Extended Data Figs. 3, 4, 8, 9), heading tuning curves were calculated by first binning heading into 35 bins centred on the visual cue positions. The voltage

trace was filtered using a median filter with a width of 40 ms to remove spikes, and the mean-filtered voltage was measured for each heading during an epoch. For heading tuning curves calculated from multiple epochs, the voltage measurement for each heading bin was weighted relative to the number of samples in each individual epoch and the mean was then taken across epochs. For display, heading tuning curves were often smoothed using a median filter with a width of two cue positions (Figs. 2c, 5b and Extended Data Figs. 3, 4, 8, 9).

Yaw during open-loop epochs. In Fig. 1e, the FicTrac yaw-position signal was unwrapped, converted into radians, low-pass filtered (Butterworth) at 25 Hz and differentiated to obtain angular velocity. On rare occasions, a value of more than 2500°s^{-1} occurred in an isolated time sample; this was probably due to imperfect nature of the unwrapping-and-differentiation procedure. These values were replaced with the value of the preceding sample. In Fig. 1f, the time-averaged yaw velocity was calculated by taking the mean yaw position during the final 250 ms of the flash and subtracting the mean yaw position during the 250 ms directly preceding the flash, and then dividing by the elapsed time (500 ms). We averaged data from left and right versions of the same cue displacement (because it seemed unlikely that a large group of flies would show a systematic bias in the right or left direction) to obtain mean yaw velocity responses to a total of 16 cue positions for each of 73 flies, thus obtaining 73×16 data points. We took the mean across flies at each cue position and plotted this as the black line in Fig. 1f. Next, to model the null case (in which visual cue position has no effect), we randomly drew 73 values (with replacement) from the matrix, without regard for cue position or fly identity, and we calculated the mean of these 73 values; we constructed a bootstrap distribution by repeating this procedure 10,000,000 times, each time calculating the mean of 73 randomly drawn values. This bootstrap distribution was used to obtain a 95% confidence interval, which was then adjusted for multiple comparisons using a Bonferroni correction ($m = 16$ tests). None of the true mean values (black) were outside this adjusted confidence interval (magenta lines). We used the same procedure in Extended Data Fig. 1e, except that the independent variable was the distance of the cue jump rather than the position of the cue. Finally, as a further control, we also examined whether any individual flies had a significant yaw velocity response to any cue position (Extended Data Fig. 1d). Because individual flies might be right- or left-handed⁵², we did not average data from right and left cue positions in this analysis; thus there were 35 cue positions. For each fly, we computed trial-averaged yaw velocity for each of 2–8 open-loop epochs, and we created a matrix containing all cue positions for every epoch in the dataset of that fly. We then randomly drew a number of values (with replacement) from the matrix (number of epochs \times 35 cue positions) to match the number of epochs that we recorded for that fly. This procedure was randomized with respect to cue position and epoch number. For each fly, a bootstrap distribution was obtained by repeating this procedure 100,000 times, each time calculating the mean of the drawn values. The difference between the observed trial-averaged yaw responses for each cue position and the mean of the bootstrap distribution was used to obtain a P value (two-sided). In this manner, a P value was calculated for every fly at every cue position (73×35 P values). The statistical significance of each trial-averaged yaw was assessed for each fly and each position at with $\alpha = 0.05$ using the Bonferroni–Holm method to correct for multiple comparisons. No tests showed a statistically significant yaw velocity for any individual fly at any cue position.

Correlations between visual receptive fields and heading turning curves in E-PG neurons. In Fig. 2c, d, heading tuning curves and visual receptive fields were smoothed using a median filter with a width of two cue positions. Correlation coefficients were computed on smoothed curves (40 pairs in total). In Fig. 2d, as a control, we randomly drew (with replacement) 40 heading tuning curves and 40 visual response

curves, yielding 40 correlation coefficients. The mean of that correlation value was then recorded. This process was repeated 10,000,000 times to build a bootstrap distribution and the 95% confidence interval of this distribution was computed.

Visual receptive fields of R neurons. In Fig. 3a, spikes were detected after low-pass filtering the recorded current at 1 kHz by identifying deflections greater than 15 pA that occurred outside a 0.5-ms refractory period. The spike rate was measured over the 500-ms visual stimulus period.

Responses of E-PG neurons to optogenetic stimulation of R neurons. In Fig. 3b, peak hyperpolarization was calculated as the trial-averaged voltage during a 1-s baseline period minus the minimum trial-averaged voltage reached in the 1 s following the 5-ms optogenetic stimulus. Four optogenetic stimulus trials were recorded per cell.

E-PG ensemble representations of heading direction. In Fig. 4, rigid motion correction in the x , y and z axes was performed for the volumetric imaging stacks for every epoch using the NoRMCorre algorithm⁵³. This algorithm performs piece-wise rigid registration of small overlapping sectors within the field of view, and then merges the sectors via interpolation, allowing approximate cancellation of non-rigid brain movement artefacts. Motion correction was parallelized on a high-performance computing cluster. For each epoch, we defined 16 regions of interest, corresponding to the 16 glomeruli in the protocerebral bridge; each region of interest was defined in one z plane. To calculate the time-dependent change in fluorescence ($\Delta F/F$) for each glomerulus, we used a baseline fluorescence (F) defined as the mean of the lowest 5% of raw fluorescence values across the entire experiment for that glomerulus. We excluded from the baseline the rare frames that were lost as a result of the rigid motion correction algorithm. The singular bump of activity in E-PG dendrites within the ellipsoid body¹ translates into two bumps in the protocerebral bridge^{3,4}; these two bumps move together, so that the signal has a spatial period of eight glomeruli in the protocerebral bridge. Therefore, to calculate the neural representation of heading direction, we took the spatial Fourier transform of $\Delta F/F$ in the protocerebral bridge across all 16 glomeruli. We used the phase of the Fourier component at eight glomeruli as the phase of the neural representation of heading for each time point; this procedure was described previously³. We used the sign convention in which a positive change in phase corresponds to a rightward movement of the bumps in the protocerebral bridge, and a clockwise movement of the bump in the ellipsoid body (when viewed from the posterior side of the brain). For display purposes only, in Fig. 4a, we averaged the $\Delta F/F$ signals from the right and left half of the protocerebral bridge (which is why only one bump is visible); this averaging was not performed as part of the data analyses described above.

Offset of the E-PG ensemble reference frame. In Fig. 4c, d, to calculate the offset of the reference frame (the difference between the fly's heading and the neural representation of heading), we first downsampled the behavioural data to match the volumetric imaging rate (6–9 Hz). We removed time points in which the FicTrac analogue signals were problematic or when the power of the Fourier transform was below a specified threshold (0.1). We also excluded the first 3 s of each 2-min closed-loop epoch due to a delay between imaging trigger and the start of the visual stimulus. We then took the angular position of the visual panorama from the analogue voltage output of the LED panel system (positive defined as to the right of the fly, or clockwise when viewed from above the set-up). We calculated the offset of the E-PG ensemble reference frame as the negative of the spatial Fourier transform phase minus the position of the visual panorama. This value is consistent with previously published methods³ to calculate the offset between the bump position in the protocerebral bridge and the ball yaw

Article

position. To quantify offset probability (Fig. 4d, f and Extended Data Fig 7), we analysed the final 4 min of each pre-training block, the full 20 min of each training block, and the first 4 min of each post-training block.

Effect of training on visual receptive fields. In Fig. 5 (and Extended Data Figs. 8, 9), heading tuning curves and visual receptive fields were smoothed using a median filter with a width of two samples (cue positions). The last pre-training open-loop epoch (probe 1) and the first post-training open-loop epoch (probe 2) were used for the following analyses. In Fig. 5d–f, the absolute change was obtained by subtracting the two visual receptive fields (post-training minus pre-training), then summing the absolute value of the difference (Δ) over all cue positions, and finally dividing by the number of positions. In Fig. 5d, the change in receptive field shape was obtained by cross-correlating probe 1 and probe 2 and calculating $1 - R^2$. In Fig. 5f, the modulation by heading during turning was taken as the difference between the maximum and the minimum of the heading direction turning curve.

Controls for training. In Fig. 5e, to estimate the drift in visual receptive field under control conditions, we had flies navigate in a one-cue world (rather than a two-cue world) during the waiting period between the open-loop epochs. In some cases (matched control in Extended Data Fig. 9), flies received exactly the same protocol as the experimental condition except with one-cue closed-loop during the training period; in other words, these matched controls received 12 consecutive minutes of one-cue (rather than two-cue) closed-loop epochs during the ‘training’ period. For other controls (control in Extended Data Fig. 9), we identified experiments from Fig. 2 in which the recording had lasted long enough for us to present four open-loop epochs interleaved with four one-cue closed-loop epochs. In these recordings, the second and fourth epochs were separated by more than 12 min (typically around 15 min) and so they are appropriate controls for the training protocol. We therefore treated the second and fourth open-loop epochs as if they were ‘probe 1’ and ‘probe 2’ epochs in a training experiment, and we analysed them as described above for the true training experiments. The important distinction is that this second group of control flies experienced one-cue rather than two-cue closed-loop epochs during the window between probe 1 and probe 2.

Data inclusion

We include epochs for Figs. 1, 2 if the cell was healthy; specifically, this meant that the epoch-averaged voltage was below -33 mV and within 15 mV of the voltage observed at the start of the first epoch of the experiment, and if the spike amplitude was more than 50% of the amplitude observed in the first epoch. Closed-loop epochs were included if the fly visited all heading directions during that epoch. Cells were included if ≥ 2 open-loop epochs met these criteria; in Fig. 2 we also required that ≥ 2 closed-loop epochs met these criteria. In Fig. 3, cells were included if ≥ 2 open-loop epochs met our cell health criteria. A single recording from the *UAS/+* control genotype was excluded because the biocytin fill showed that it was not an E-PG neuron. All other biocytin-filled neurons analysed during this project (that is, 65 out of 66 neurons) were confirmed to be E-PG neurons. All recordings that were not imaged post hoc were therefore assumed to target E-PG cells. We excluded 5 out of 24 flies in Fig. 4 owing to either weak fluorescence or an unstable offset between the angle of the E-PG bump and the fly’s heading angle at the end of the initial closed-loop one-cue epoch. In Fig. 5, cells were included if the epoch-averaged voltage from all epochs of the experiment (pre-training, training, post-training) was below -33 mV and if the fly visited all heading directions during the two epochs (8 min) of one-cue closed-loop before training and during the final two epochs (8 min) of two-cue closed-loop training. We required that the fly’s mean yaw velocity was $>20^\circ/\text{s}$ during the final 2 epochs of the two-cue closed-loop training; 10 cells were excluded due to this restriction.

We also removed recordings in which the visual receptive field and/or heading turning curve were almost flat during the pre-training period ($\max - \min \leq 2$ mV); six cells were removed due to this restriction.

On occasion, during E-PG neuron electrophysiological recordings, we observed unexpected large inhibitory postsynaptic potentials with a stereotyped sharp onset, a large amplitude (>15 mV) and a stereotyped time course. They were followed by a prolonged period of depolarization when the variance of the voltage trace was also diminished. These events interfered with visual and heading tuning measurements; therefore, for Figs. 1–3, any epoch in which such an event occurred was excluded from the analysis. For Fig. 5, the event was clipped but the rest of the epoch was used; 5% of open loop epochs and 10% of closed-loop epochs were clipped in this manner.

Analysis was performed using MATLAB R2016b, R2017a and R2017b (MathWorks).

Determination of sample sizes

For genetic perturbation experiments (Fig. 3c), the number of experiments performed was determined by first collecting a pilot dataset of ($n = 4$ for the three genotypes using the *R2OA02-Gal4* driver line). On the basis of the initial effect size, power analysis was used to determine the number of experiments needed to test the hypothesis that visually evoked hyperpolarization was smaller in the experimental genotype. For all other experiments, sample sizes were chosen based on standard sample sizes in the field.

Reporting summary

Further information on research design is available in the Nature Research Reporting Summary linked to this paper.

Data availability

The datasets generated during and/or analysed during the current study are available from the corresponding author on reasonable request.

Code availability

Analysis code is available at https://github.com/wilson-lab/FisherLu-DAlessandroWilson_AnalysisCode.

37. Jenett, A. et al. A GAL4-driver line resource for *Drosophila* neurobiology. *Cell Rep.* **2**, 991–1001 (2012).
38. Wang, J., Zugates, C. T., Liang, I. H., Lee, C. H. & Lee, T. *Drosophila* Descam is required for divergent segregation of sister branches and suppresses ectopic bifurcation of axons. *Neuron* **33**, 559–571 (2002).
39. Pfeiffer, B. D. et al. Refinement of tools for targeted gene expression in *Drosophila*. *Genetics* **186**, 735–755 (2010).
40. Hooper, E. D., Jung, Y., Inagaki, H. K., Rubin, G. M. & Anderson, D. J. P1 interneurons promote a persistent internal state that enhances inter-male aggression in *Drosophila*. *eLife* **4**, e11346 (2015).
41. Hardie, R. C. et al. Calcium influx via TRP channels is required to maintain PIP₂ levels in *Drosophila* photoreceptors. *Neuron* **30**, 149–159 (2001).
42. Chen, T. W. et al. Ultrasensitive fluorescent proteins for imaging neuronal activity. *Nature* **499**, 295–300 (2013).
43. Nern, A., Pfeiffer, B. D. & Rubin, G. M. Optimized tools for multicolor stochastic labeling reveal diverse stereotyped cell arrangements in the fly visual system. *Proc. Natl. Acad. Sci. USA* **112**, E2967–E2976 (2015).
44. Goodman, M. B. & Lockery, S. R. Pressure polishing: a method for re-shaping patch pipettes during fire polishing. *J. Neurosci. Methods* **100**, 13–15 (2000).
45. Green, J., Vijayan, V., Mussells Pires, P., Adachi, A. & Maimon, G. Walking *Drosophila* aim to maintain a neural heading estimate at an internal goal angle. Preprint at <https://doi.org/10.1101/315796> (2018). If ref. 45 (preprint) has now been published in final peer-reviewed form, please update the reference details if appropriate. If ref. 45 has now been accepted or published in peer-reviewed form, please update the reference.
46. Gouwens, N. W. & Wilson, R. I. Signal propagation in *Drosophila* central neurons. *J. Neurosci.* **29**, 6239–6249 (2009).
47. Wolff, T., Iyer, N. A. & Rubin, G. M. Neuroarchitecture and neuroanatomy of the *Drosophila* central complex: a GAL4-based dissection of protocerebral bridge neurons and circuits. *J. Comp. Neurol.* **523**, 997–1037 (2015).
48. Moore, R. J. et al. FictTrac: a visual method for tracking spherical motion and generating fictive animal paths. *J. Neurosci. Methods* **225**, 106–119 (2014).
49. Reiser, M. B. & Dickinson, M. H. A modular display system for insect behavioral neuroscience. *J. Neurosci. Methods* **167**, 127–139 (2008).

50. Klapoetke, N. C. et al. Independent optical excitation of distinct neural populations. *Nat. Methods* **11**, 338–346 (2014).
51. Schindelin, J. et al. Fiji: an open-source platform for biological-image analysis. *Nat. Methods* **9**, 676–682 (2012).
52. Buchanan, S. M., Kain, J. S. & de Bivort, B. L. Neuronal control of locomotor handedness in *Drosophila*. *Proc. Natl Acad. Sci. USA* **112**, 6700–6705 (2015).
53. Pnevmatikakis, E. A. & Giovannucci, A. NoRMCorre: an online algorithm for piecewise rigid motion correction of calcium imaging data. *J. Neurosci. Methods* **291**, 83–94 (2017).

Acknowledgements We thank D. Anderson, T. Clandinin, B. Pfeiffer, G. Rubin and J. Tuthill for providing fly stocks; T. Clandinin, B. Bean, J. Drugowitsch, D. Ginty and members of the Wilson laboratory for providing feedback on the manuscript and J. Drugowitsch for providing advice on data analysis; G. Maimon for sharing designs for a fly holder and modified FicTrac software; O. Mazor and P. Górelkí at the Harvard Medical School Research Instrumentation Core (NEI Core Grant for Vision Research EY012196) for their help constructing the virtual-reality systems. This work was supported by the Harvard Neurobiology Imaging Facility (NINDS P30 NS072030). This work was funded by NIH awards U19NS104655, F30DC017698 (to J.L.) and

T32GM007753 (to J.L.). Y.E.F. is supported by a HHMI Hanna H. Gray Fellowship. R.I.W. is an HHMI Investigator.

Author contributions Y.E.F., J.L. and R.I.W. designed the study. Y.E.F. performed and analysed electrophysiology experiments. J.L. performed and analysed two-photon calcium-imaging experiments. I.D. performed and analysed confocal-microscopy imaging experiments. Y.E.F. and R.I.W. wrote the manuscript with input from J.L. and I.D.

Competing interests The authors declare no competing interests.

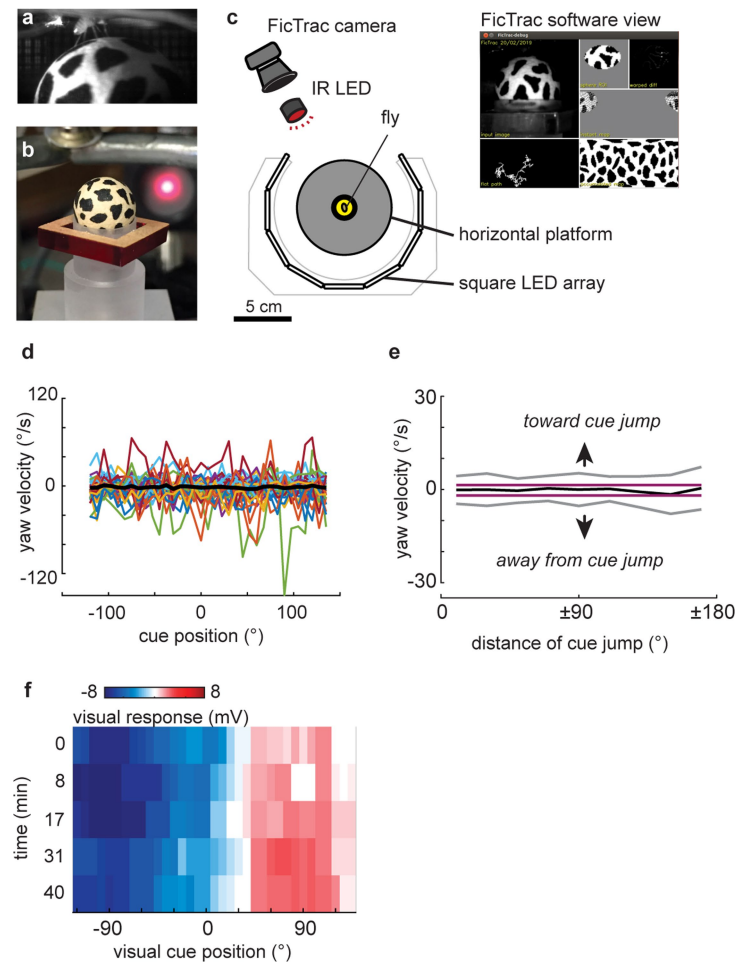
Additional information

Supplementary information is available for this paper at <https://doi.org/10.1038/s41586-019-1772-4>.

Correspondence and requests for materials should be addressed to R.I.W.

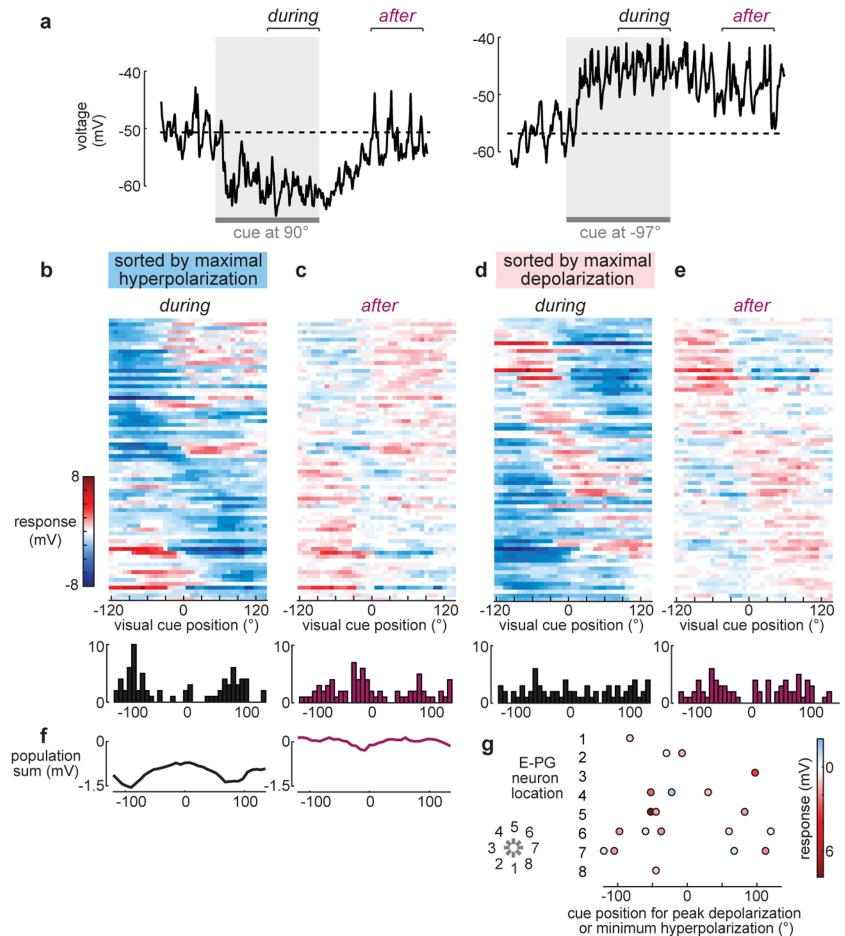
Peer review information *Nature* thanks Lisa Giocomo and the other, anonymous, reviewer(s) for their contribution to the peer review of this work.

Reprints and permissions information is available at <http://www.nature.com/reprints>.


Extended Data Fig. 1 | Measuring behaviour and E-PG visual responses.

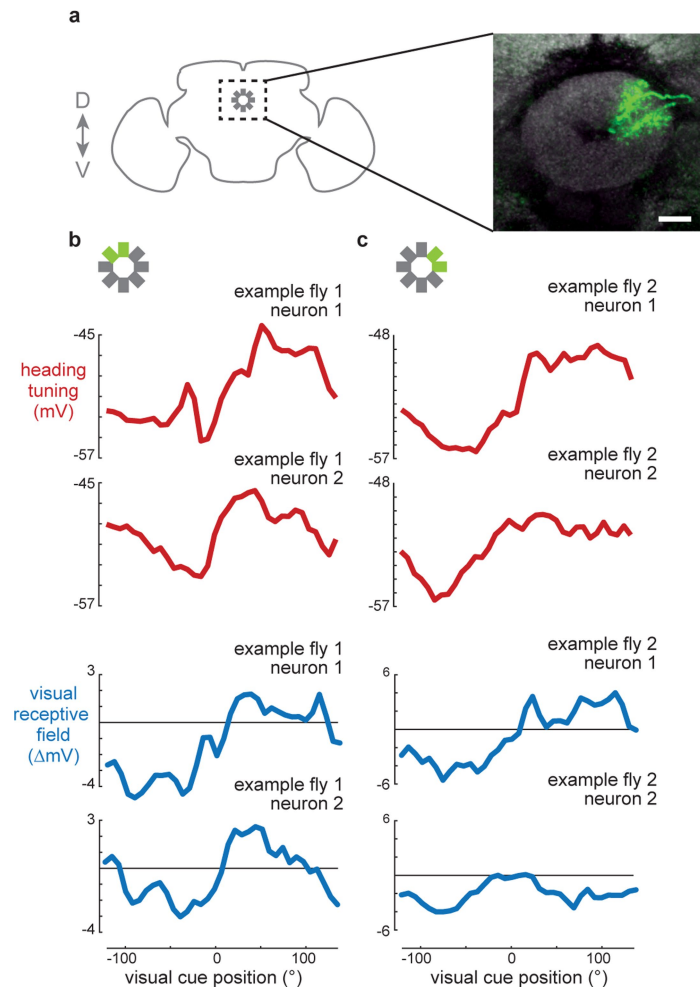
a, Side view of a fly walking on an air-cushioned ball during an electrophysiology experiment. **b**, Image of the ball and plastic holder. Air flows up through the holder and out the semi-spherical depression that cradles the ball. **c**, Schematic of the experimental set-up viewed from above. The fly is secured in an aperture in the centre of a horizontal platform. The platform is surrounded by a circular panorama. The panorama is composed of square LED arrays⁴⁹ (2 squares vertically \times 12 squares horizontally). The ball is illuminated by an infrared (IR) LED, which is visible as a red spot in **b**. A camera captures an image of the ball to enable tracking using FicTrac⁴⁸. Inset shows FicTrac view. Camera and infrared LED are not drawn to scale. **d**, The yaw velocity of the fly compared to the cue position. This is the dataset that is the basis for Fig. 1f, but here broken down into averages for each individual fly, and with right (+) and left (-) cue positions kept separate. Positive velocities are right turns, and negative velocities are left turns. No tests showed a statistically significant yaw velocity ($P < 0.05$, two-sided comparison to bootstrap distribution) for any individual fly at any cue position. For details of analysis, see Methods, 'Yaw

during open-loop epochs'. **e**, Yaw velocity in response to the visual cue presentation. This analysis is the same as that shown in Fig. 1f, but here yaw velocity is plotted against the distance of the cue jump between consecutive trials. As in Fig. 1f, we show mean (black) \pm 1 s.d. (grey) across experiments (73 experiments in 68 flies). Magenta lines show the bootstrapped 95% confidence interval of the mean across flies after randomizing cue positions, Bonferroni-corrected for multiple comparisons. Because the mean lies within these bounds, it is not significantly different from random. This analysis further supports the conclusion that there is no systematic yaw response to the random flashes of the vertical bar. For details of analysis, see Methods, 'Yaw during open-loop epochs'. **f**, The visual receptive field of an example cell measured multiple times over the course of a 40-min recording. Each row shows data from a separate visual mapping epoch. Data from this example cell are also shown in Fig. 1e. Note the stability of the visual receptive field over this time period. For experiments shown in this figure, we used *UAS-mCD8::GFP/UAS-mCD8::GFP; R60D05-Gal4/R60D05-Gal4* flies.



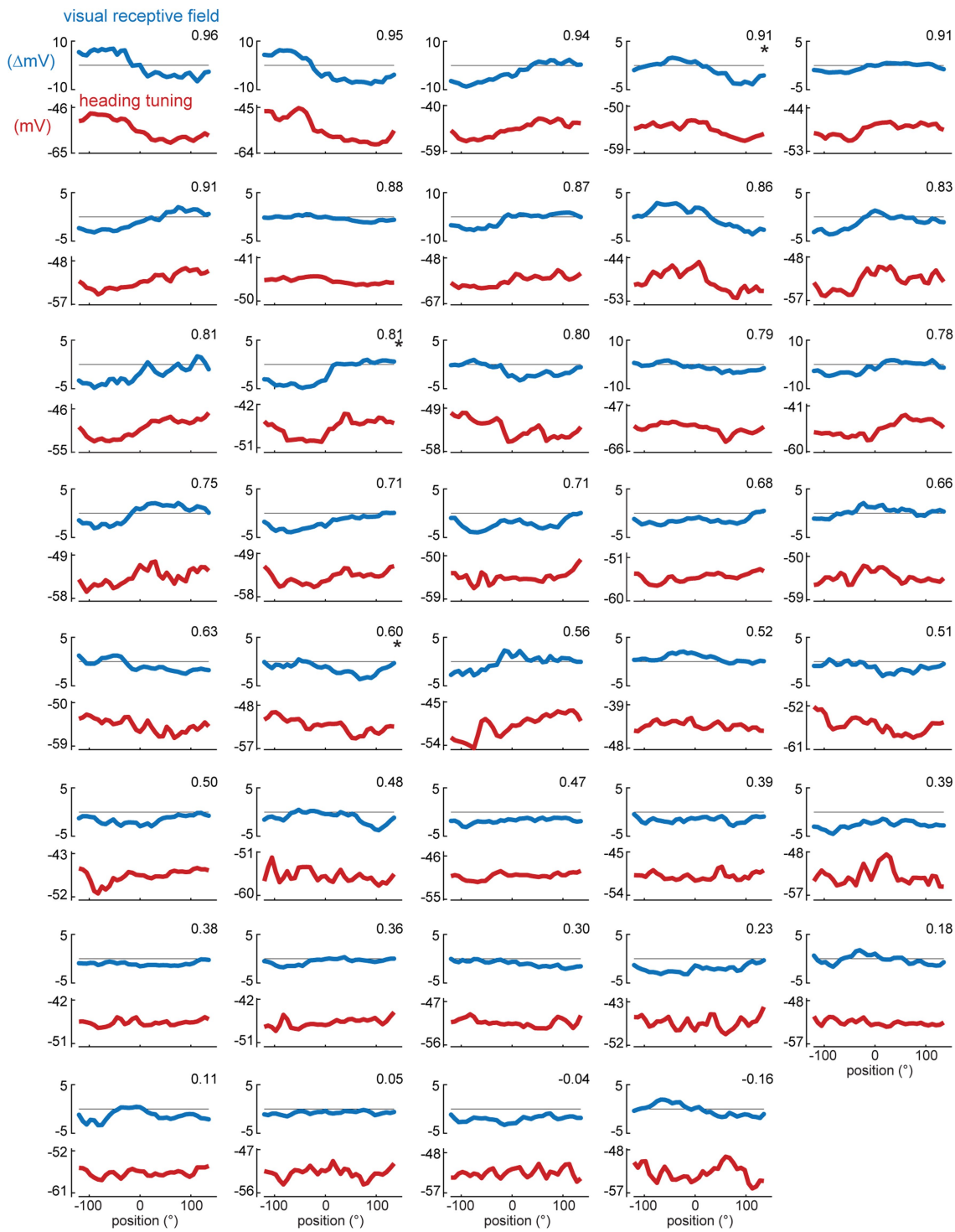
Extended Data Fig. 2 | Visually evoked hyperpolarization and depolarization, during and after cue presentation. **a**, Example voltage responses of the same E-PG neuron to two cue positions. Dashed lines indicate the mean baseline voltage before the cue. This neuron is hyperpolarized by the cue at 90° and depolarized by the cue at -97°. Note that hyperpolarization decays more rapidly than depolarization. In **b**, to quantify visual receptive fields, we measured the change in voltage during cue presentation and after cue removal in the 250-ms windows marked in **a** with brackets, in both cases relative to baseline. **b**, Summary of E-PG visual receptive fields measured during cue presentation. Cells are sorted by the cue position that evokes maximal hyperpolarization. The histogram shows the number of E-PG neurons with maximal hyperpolarization at each cue position (73 E-PG neurons in 68 flies). **c**, Summary of E-PG visual receptive fields measured after cue removal. Cell order is the same as in **b**. Note that hyperpolarizing responses tend to decay, whereas depolarizing responses tend to persist; this is consistent with the hypothesis that the hyperpolarization during cue presentation is due to

direct synaptic inhibition from R neurons, whereas depolarization is polysynaptic and caused by withdrawal of tonic synaptic inhibition. The histogram shows the number of E-PG neurons with maximal hyperpolarization after cue removal for each cue position. **d**, Same as **b**, but sorted by the cue position that evoked maximal depolarization (minimal hyperpolarization), as in Fig. 1g. **e**, Same as **c**, but with the cell order as in **d**. **f**, Summed response across all neurons measured during (left) and after (right) the cue. The left curve has a pair of minima around $\pm 100^\circ$; this bias is probably inherited from R neuron receptive fields, which are biased towards positions offset from the visual midline⁵. By contrast, the right curve is relatively flat. **g**, Visual cue position eliciting maximal depolarization (minimum hyperpolarization), plotted versus E-PG neuron location, for the 21 recorded E-PG neurons that were filled. No significant correlation was observed (circular correlation coefficient = -0.15, $P = 0.49$)³⁶. For experiments shown in this figure, we used *UAS-mCD8::GFP/UAS-mCD8::GFP; R60D05-Gal4/R60D05-Gal4* flies.



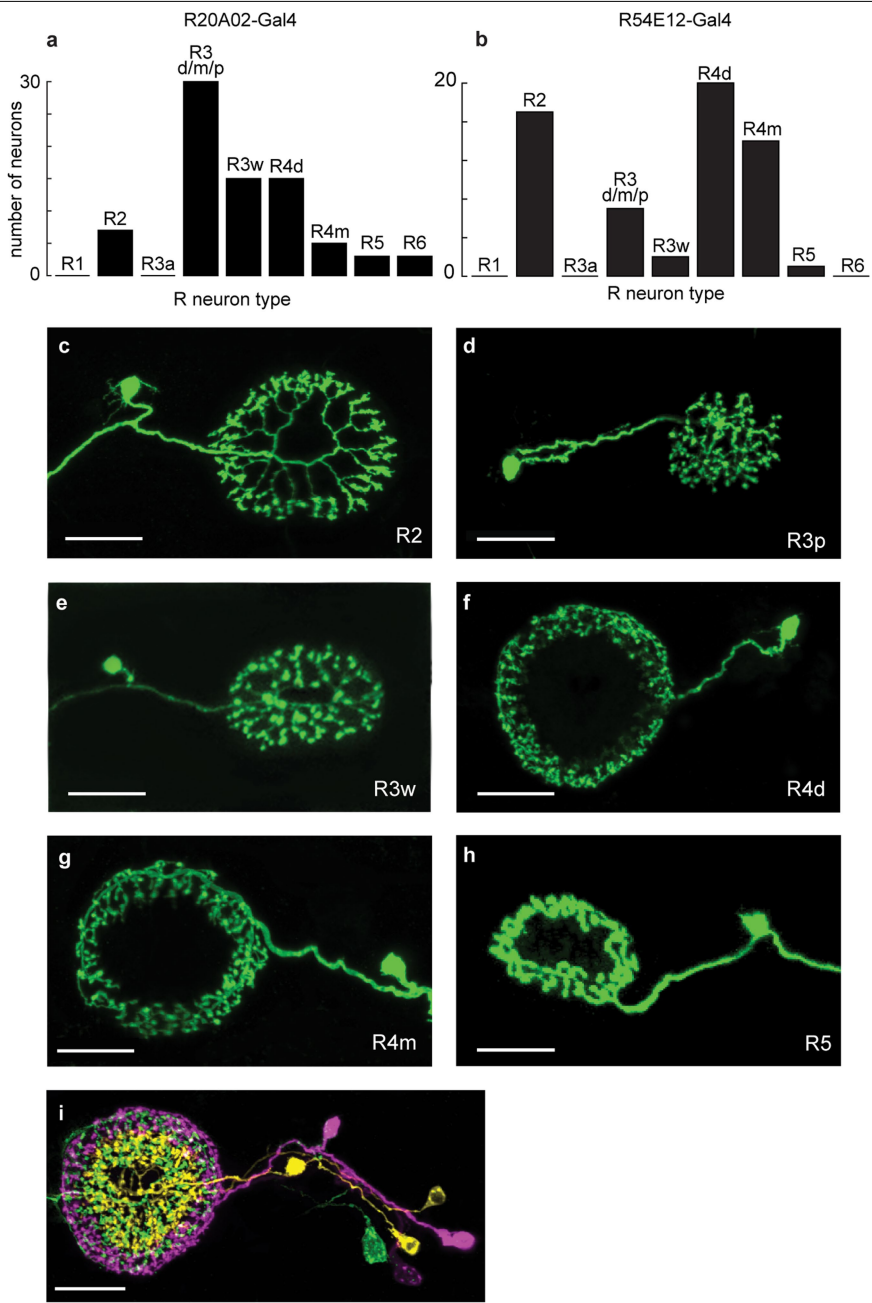
Extended Data Fig. 3 | E-PG neuron pairs recorded sequentially from the same brain. **a.** Two biocytin filled dendrites (green) from sequentially recorded E-PG neurons that innervate adjacent wedges within the ellipsoid body. Neuropil reference marker is shown in grey (anti-nc82 antibody). Images are maximum intensity z-projections. Scale bar, 10 μ m. The schematic shows the approximate position of ellipsoid body and E-PG dendrites from a coronal view of the fly brain. **b, c.** Heading tuning (red, measured in VR) and visual receptive field (blue, measured with random flashes) from sequentially recorded E-PG pairs from two example flies. Dendritic locations of the recorded neurons are green in the ellipsoid body schematic above each set of

plots. In both cases, by chance, the two dendrites were physically adjacent. In both cases, adjacent E-PG neurons from the same fly exhibited similar visual receptive fields and heading tuning curves, supporting the conclusion that adjacent E-PG cells typically receive inhibition from adjacent regions of visual space and represent adjacent heading directions. Comparing the visual receptive field and the heading tuning curve for each neuron yielded correlation coefficients (Pearson's) of 0.76 (fly 1 neuron 1), 0.90 (fly 1 neuron 2), 0.95 (fly 2 neuron 1) and 0.65 (fly 2 neuron 2). For experiments shown in this figure, we used *UAS-mCD8::GFP/UAS-mCD8::GFP; R60D05-Gal4/R60D05-Gal4* flies.



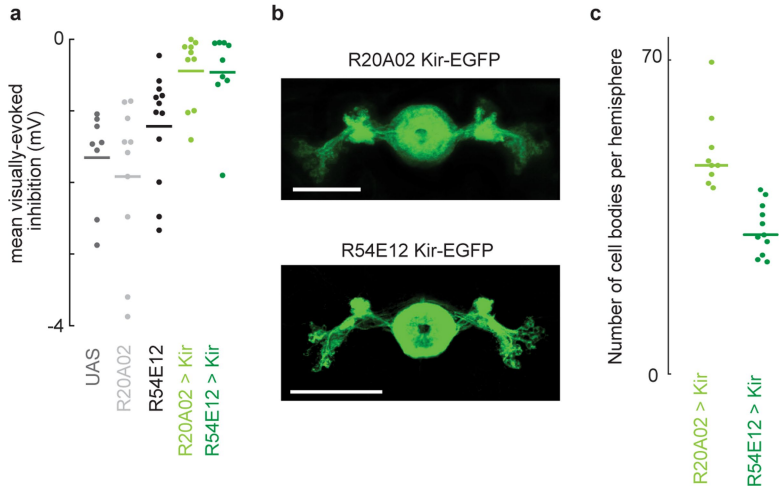
Extended Data Fig. 4 | Visual receptive fields and heading tuning of E-PG neurons. Heading tuning (red, closed-loop mode) and visual receptive fields (blue, open-loop mode) for all 40 recorded E-PG neurons (from 39 flies). For each neuron, the correlation coefficient (Pearson's) is reported for the

comparison between the visual receptive field and the heading tuning curve. Asterisks denote data also shown in Fig. 2. For experiments shown in this figure, we used *UAS-mCD8::GFP/UAS-mCD8::GFP; R60D05-Gal4/R60D05-Gal4* flies.



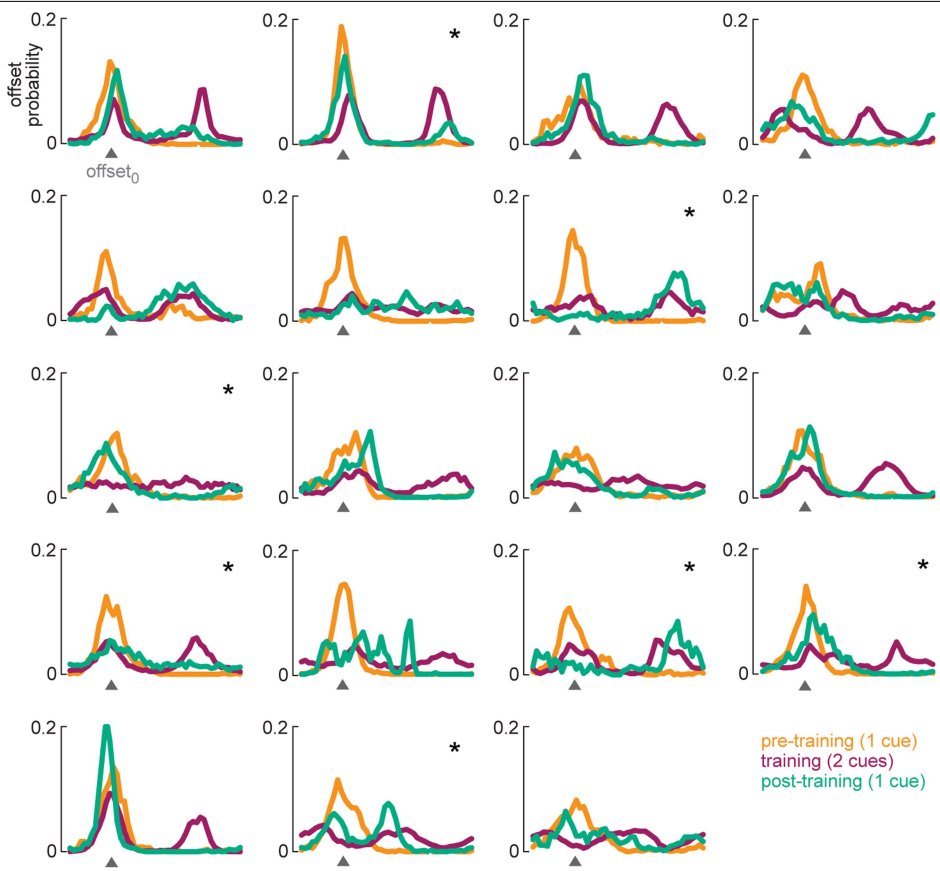
Extended Data Fig. 5 | R neurons types labelled by *R20A02-Gal4* and *R54E12-Gal4* described by MCFO. **a**, Observed numbers of R neurons belonging to each type from a dataset of $n=78$ single-neuron MCFO clones⁴³ from the *R20A02-Gal4* line. R neuron types were classified according previously published methods⁶. **b**, Same as in **a** but for the *R54E12-Gal4* line ($n=61$ single-neuron MCFO clones). **c–h**, Examples of single R neuron MCFO clones. Images are maximum intensity z-projections. Background labelling was manually

removed to improve clarity of specific neuronal morphologies. **i**, Multiple R neuron MCFO clones labelled in different colours using the *R20A02-Gal4* line. Image is a maximum-intensity z-projection. Scale bars, 20 μm . For experiments shown in this figure, we used *R57C10-FLPG5.PEST; UAS(FRT.stop)myr::smGdP-HA*, *UAS(FRT.stop)myr::smGdP-V5*, *UAS(FRT.stop)myr::smGdP-Flag/R20A02-Gal4*, *R57C10-FLPG5.PEST; UAS(FRT.stop)myr::smGdP-HA*, *UAS(FRT.stop)myr::smGdP-V5*, *UAS(FRT.stop)myr::smGdP-Flag/R54E12-Gal4* flies.



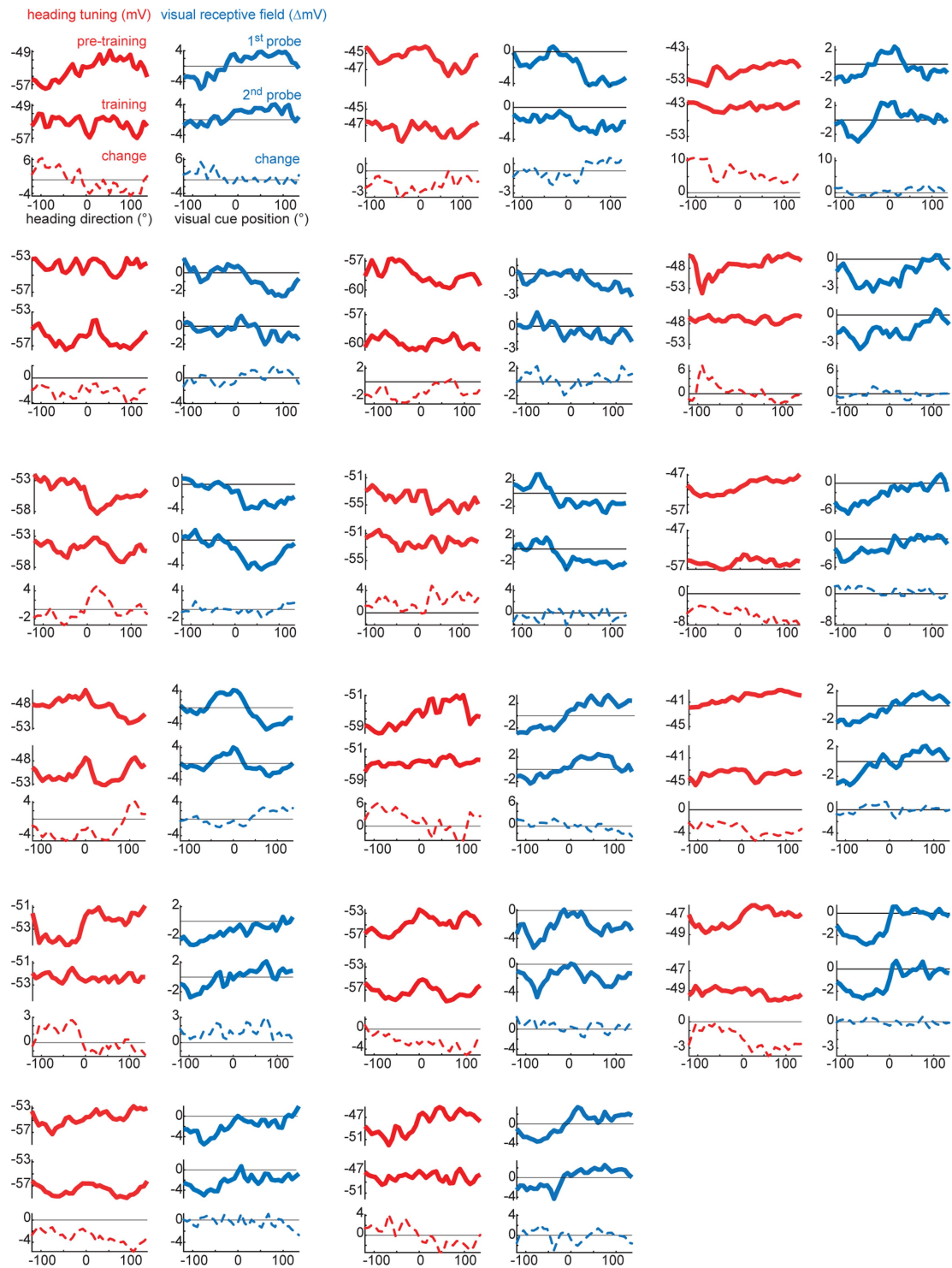
Extended Data Fig. 6 | Suppressing R neuron activity with two independent driver lines reduces visually evoked hyperpolarization in E-PG neurons.
a, Same as Fig. 3c, except instead of measuring peak visually evoked hyperpolarization, we measured mean visually evoked hyperpolarization (by zeroing all non-negative visual responses and then averaging visual responses across all cue positions). From left to right: $n = 8, 10, 12, 10, 9$. Both Kir2.1 means are significantly different from corresponding genetic controls using two-sided Wilcoxon rank-sum tests. *R20A02* Kir2.1 versus *R20A02*/ $+$ and *UAS*/ $+$ ($P = 0.0013$ and $P = 0.0003$, respectively), *R54E12* Kir2.1 versus *R54E12*/ $+$ and *UAS*/ $+$ ($P = 0.005$ and $P = 0.0025$, respectively). **b**, R neuron population labelled by Kir2.1::eGFP. Images are maximum intensity z-projections. **c**, Numbers of R neurons per hemisphere expressing Kir2.1::eGFP in each experimental genotype, $n = 9$ (*R20A02*) and $n = 11$ (*R54E12*) (horizontal lines are means). On the basis of the previously reported total number of R neurons of each type⁶ and our MCFO quantification of the R neuron types labelled by *R20A02*-Gal4 and *R54E12*-Gal4 (Extended Data Fig. 5), these cell counts suggest that *R20A02*-

Gal4 targets approximately 20% of R2, 30% of R4m and all R4d neurons. These counts suggest that *R54E12*-Gal4 targets approximately 40% of R2 neurons and all R4m and R4d neurons. This incomplete targeting of outer R neurons may provide one explanation for the remaining visually evoked inhibition observed in some recordings (Fig. 3). Note that although both driver lines label other neurons in the central brain and visual system, R neurons appear to be the only cell type that is labelled by both lines. In the visual system, the driver line *R20A02*-Gal4 targets one medulla intrinsic neuron, probably Mi12, and one cell type that arborizes in around layers 4–6 of the lobula, whereas the driver line *R54E12*-Gal4 appears to target the medulla neuron Tm3. For experiments shown in this figure, we used +/*w*; *R60D05-LexA/LexAop-mCD8::GFP*; +/*UAS-Kir2* (*UAS*-only control); +/*w*; *R60D05-LexA/LexAop-mCD8::GFP*; *R20A02-Gal4*/ $+$ (*R20A02* Gal4-only control); +/*w*; *R60D05-LexA/LexAop-mCD8::GFP*; *R54E12-Gal4*/ $+$ (*R54E12* Gal4-only control); +/*w*; *R60D05-LexA/LexAop-mCD8::GFP*; *R20A02-Gal4/UAS-Kir2.1* (*R20A02* Kir2.1); and +/*w*; *R60D05-LexA/LexAop-mCD8::GFP*; *R54E12-Gal4/UAS-Kir2.1* (*R54E12* Kir2.1) flies.



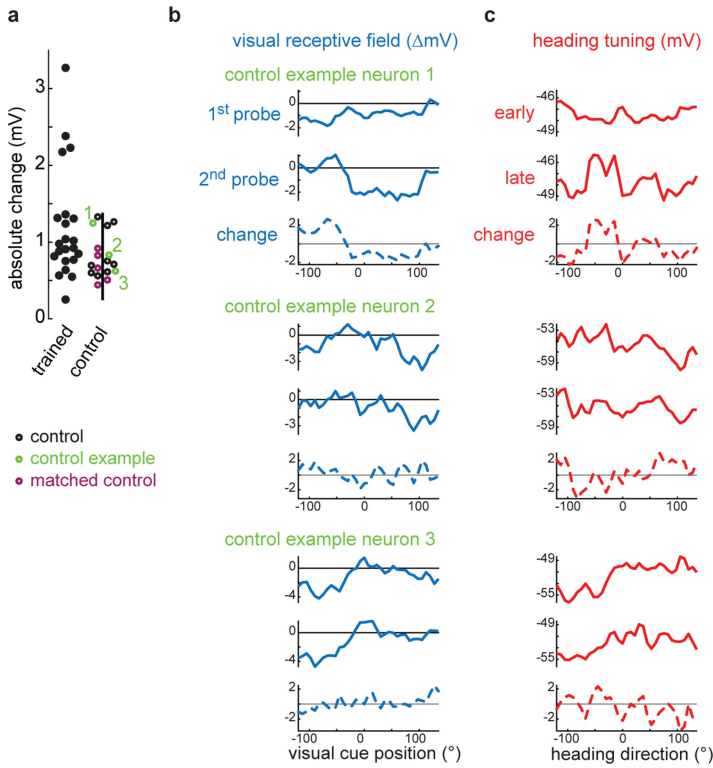
Extended Data Fig. 7 | Offset probability histograms in training experiments. Offset probability histograms during each segment of the training experiments shown in Fig. 4, for all 19 GCaMP imaging experiments (in 19 flies). As in Fig. 4, the circular mean during the pre-training period is defined

as offset_0 (here marked with an arrowhead), and for display purposes we horizontally aligned all of the offset_0 values in different flies. Asterisks mark data shown in Fig. 4. For experiments shown in this figure, we used $+/\text{w}; \text{UAS-GCaMP6f}/+; \text{R60D05-Gal4}/+$ flies.



Extended Data Fig. 8 | Heading tuning and visual receptive field measurements in training experiments. Heading tuning curves and visual receptive fields for all additional 17 E-PG neurons (from 17 flies) from the training experiments in Fig. 5. As in Fig. 5, red solid curves are heading tuning.

The red dashed curves are the change in heading tuning (training minus pre-training). Blue curves are visual receptive fields. The blue dashed curve is the change in the visual receptive field (second probe minus first probe). Seven neurons from this dataset are also shown in Figs. 1, 2.



Extended Data Fig. 9 | Controls for remapping experiments. **a**, Data reproduced from Fig. 5e. Absolute change in visual receptive fields. Control flies navigated in a one-cue world (rather than a two-cue world) during the waiting period between the open-loop epochs used to compute the change in visual responses. In some cases (matched control), flies received exactly the same protocol as the experimental condition except with one-cue closed-loop epochs during the training period; in other words, these matched controls received 12 consecutive minutes of one-cue (rather than two-cue) closed-loop epochs during the training period. In all other cases (control), flies received 4-min blocks of one-cue closed-loop epochs interleaved with 150-s open-loop epochs during the training period, which lasted 12 min or more. **b**, Visual

receptive fields from control cells. Blue dashed curve is the change in visual receptive field (second probe minus first probe) over the control period. Typically, visual receptive fields were stable over time under control conditions (control neurons 2 and 3). On occasion, we observed spontaneous changes in the visual receptive field of an E-PG neuron during the control period (for example, control neuron 1), although these changes were not as large as the changes that we observed in many neurons in trained flies (see **a**). **c**, Heading tuning in the same three control cells. Note how the spontaneous changes in visual receptive fields seen in neuron 1 are accompanied by changes in heading tuning.

Corresponding author(s): Rachel Wilson

Last updated by author(s): Sept 12, 2019

Reporting Summary

Nature Research wishes to improve the reproducibility of the work that we publish. This form provides structure for consistency and transparency in reporting. For further information on Nature Research policies, see [Authors & Referees](#) and the [Editorial Policy Checklist](#).

Statistics

For all statistical analyses, confirm that the following items are present in the figure legend, table legend, main text, or Methods section.

n/a Confirmed

- The exact sample size (n) for each experimental group/condition, given as a discrete number and unit of measurement
- A statement on whether measurements were taken from distinct samples or whether the same sample was measured repeatedly
- The statistical test(s) used AND whether they are one- or two-sided
Only common tests should be described solely by name; describe more complex techniques in the Methods section.
- A description of all covariates tested
- A description of any assumptions or corrections, such as tests of normality and adjustment for multiple comparisons
- A full description of the statistical parameters including central tendency (e.g. means) or other basic estimates (e.g. regression coefficient) AND variation (e.g. standard deviation) or associated estimates of uncertainty (e.g. confidence intervals)
- For null hypothesis testing, the test statistic (e.g. F , t , r) with confidence intervals, effect sizes, degrees of freedom and P value noted
Give P values as exact values whenever suitable.
- For Bayesian analysis, information on the choice of priors and Markov chain Monte Carlo settings
- For hierarchical and complex designs, identification of the appropriate level for tests and full reporting of outcomes
- Estimates of effect sizes (e.g. Cohen's d , Pearson's r), indicating how they were calculated

Our web collection on [statistics for biologists](#) contains articles on many of the points above.

Software and code

Policy information about [availability of computer code](#)

Data collection

Matlab 2016a, Matlab 2017a, Matlab 2017b, ScanImage 2017, Fiji (<https://fiji.sc/>), FicTrac (<http://rjdmoore.net/fictrac/>)

Data analysis

All analyses of calcium imaging and electrophysiology data were performed using custom code written in Matlab 2017b (electrophysiology) and Matlab 2016b (calcium imaging) (see Methods for full description of analysis, code is available at https://github.com/wilson-lab/FisherLuDAlessandroWilson_AnalysisCode). Confocal images were analyzed using Fiji (ImageJ) and cell body counting was performed using the Fiji Cell Counter plugin (Schindelin, J. et al. Fiji: an open-source platform for biological-image analysis. Nat Methods 9, 676-682, (2012).)

For manuscripts utilizing custom algorithms or software that are central to the research but not yet described in published literature, software must be made available to editors/reviewers. We strongly encourage code deposition in a community repository (e.g. GitHub). See the Nature Research [guidelines for submitting code & software](#) for further information.

Data

Policy information about [availability of data](#)

All manuscripts must include a [data availability statement](#). This statement should provide the following information, where applicable:

- Accession codes, unique identifiers, or web links for publicly available datasets
- A list of figures that have associated raw data
- A description of any restrictions on data availability

The datasets generated during and/or analyzed during the current study are available from the corresponding author on reasonable request.

Field-specific reporting

Please select the one below that is the best fit for your research. If you are not sure, read the appropriate sections before making your selection.

Life sciences Behavioural & social sciences Ecological, evolutionary & environmental sciences

For a reference copy of the document with all sections, see nature.com/documents/nr-reporting-summary-flat.pdf

Life sciences study design

All studies must disclose on these points even when the disclosure is negative.

Sample size	For genetic perturbation experiments (Fig. 3c), the number of experiments performed was determined by first collecting a pilot data set ($n=4$ for each of the 3 genotypes using the R20A02-Gal4 driver line). Based on the initial effect size, power analysis was used to determine the number of experiments needed to test the hypothesis that visually-evoked inhibition was smaller in the experimental genotype. For all other experiments, sample sizes were chosen based on standard sample sizes in the field.
Data exclusions	Figs. 1 & 2: Epochs were included if the cell was healthy; specifically, this meant that the epoch-averaged voltage was below -33 mV and within 15 mV of the voltage observed at the start of the first epoch of the experiment, and also if the spike amplitude was >50% of the amplitude observed in the first epoch. Closed-loop epochs were included if the fly visited all heading directions during that epoch. Cells were included if ≥ 2 open-loop epochs met these criteria; in Fig. 2 we also required that ≥ 2 closed-loop epochs met these criteria. Fig. 3: Cells were included if ≥ 2 open-loop epochs met our cell health criteria. A single recording from the UAS/+ control genotype was excluded because the biocytin fill showed that it was not an E-PG neuron. Fig. 4: 5/24 flies were excluded due to either weak fluorescence or an unstable offset between the angle of the E-PG bump and the fly's heading angle at the end of the initial closed-loop 1-cue epoch. Fig. 5: Cells were included if the epoch-averaged voltage from all epochs of the experiment (pre-training, training, post-training) was <-33 mV, and if the fly visited all heading directions during the 2 epochs (8 min) of 1-cue closed-loop prior to training and during the final 2 epochs (8 min) of 2-cue closed-loop training. We required that the fly's mean yaw velocity was $>20^\circ/\text{s}$ during the final 2 epochs of the 2-cue closed-loop training; 10 cells were excluded due to this restriction. We also removed recordings where the visual and/or heading turning curves were almost flat during the pre-training period (max-min $\leq 2\text{mV}$); 6 cells were removed due to this restriction. On occasion, during E-PG neuron electrophysiological recordings, we observed unexpected large inhibitory postsynaptic potentials with a stereotyped sharp onset, a large amplitude ($>15\text{mV}$), and a stereotyped time course. They were followed by a prolonged period of depolarization when the variance of the voltage trace was also diminished. These events interfered with visual and heading tuning measurements, and so for Figs. 1-3, any epoch where such an event occurred was excluded from the analysis. For Fig. 5, the event was clipped but the rest of the epoch was used; 5% of open loop epochs and 10% of closed-loop epochs were clipped in this manner.
Replication	For genetic perturbation experiments (Fig 3c) we reproduced the effect of R neuron silencing with two independent driver lines (R20A02 and R54E12). For all other experiments, results were replicated in different individuals within each data set.
Randomization	For genetic perturbation experiments (Fig 3c) flies were grouped based on genotype (neuronal activity manipulated by Kir2.1 expression vs control genotypes). For comparison between trained and control flies (Fig 5) the experimental protocol that would be performed (control vs training) was always decided on prior to starting the experiment. No other randomization was performed.
Blinding	The experimenter was not blind to genotype except when genetic perturbations were used: Figure 3c (Kir2.1 perturbation). For the Figure 3c data set collected for driver line R20A02-Gal4 the experimenter was blind to genotype after the pilot phase; because Fig. 3c pilot data were indistinguishable from subsequent data, all data were ultimately pooled, and overall the experimenter was blind to genotype in 67% of these recordings. For the data set obtained using the driver line R54E12-Gal4, the experimenter was not blind to genotype because the experimental genotype was obtained at a lower-than expected (sub-Mendelian) frequency, making it impractical to blind the experimenter.

Reporting for specific materials, systems and methods

We require information from authors about some types of materials, experimental systems and methods used in many studies. Here, indicate whether each material, system or method listed is relevant to your study. If you are not sure if a list item applies to your research, read the appropriate section before selecting a response.

Materials & experimental systems

n/a	Involved in the study
<input type="checkbox"/>	<input checked="" type="checkbox"/> Antibodies
<input checked="" type="checkbox"/>	<input type="checkbox"/> Eukaryotic cell lines
<input checked="" type="checkbox"/>	<input type="checkbox"/> Palaeontology
<input type="checkbox"/>	<input checked="" type="checkbox"/> Animals and other organisms
<input checked="" type="checkbox"/>	<input type="checkbox"/> Human research participants
<input checked="" type="checkbox"/>	<input type="checkbox"/> Clinical data

Methods

n/a	Involved in the study
<input checked="" type="checkbox"/>	<input type="checkbox"/> ChIP-seq
<input checked="" type="checkbox"/>	<input type="checkbox"/> Flow cytometry
<input checked="" type="checkbox"/>	<input type="checkbox"/> MRI-based neuroimaging

Antibodies

Antibodies used

- rat anti-FLAG (Novus Biologicals), Cat#: NBP1-06712B, RRID: AB_10006034, clone#: L5, lot#: B-3
- rabbit anti-HA (Cell Signaling Technologies), Cat#: 3724 RRID: AB_1549585, clone#: C29F4, lot#: 9
- DyLight 550-conjugated mouse anti-V5 (Bio-Rad), Cat#: MCA1360D550GA, RRID: AB_2687576, clone#: SV5-Pk1
- mouse anti-Bruchpilot antibody (Developmental Studies Hybridoma Bank, nc82), Cat#: nc82, RRID: AB_2314866
- chicken anti-GFP (Abcam), Cat#: ab13970, RRID: AB_300798

Validation

Multi-colorFlip Out (MCFO) immunohistochemistry:

Multi-colorFlip Out (MCFO) genetic strategy (Nern et al. 2015) uses expression of epitopes (HA, FLAG and V5) that are not endogenous to the fly genome. For MCFO immunostaining in our study we followed the exact protocol as established and validated in Drosophila by Nern et al. that uses anti-HA, anti-FLAG and anti-V5 antibodies (Nern et al. 2015). These antibodies have also each been validated prior to Nern et al.:

rat anti-FLAG: Manufacturer notes confirms that rat anti-FLAG (Cat#: NBP1-06712B) has also been validated as FLAG-Tag specific in Drosophila (PMID: 26573957).

rabbit anti-HA: Manufacturer confirmed rabbit anti-HA antibody has Epitope tag specificity using western blot and immunohistochemical analysis comparing untransfected with HA-tag transfected COS cells (<https://www.cellsignal.com/products/primary-antibodies/ha-tag-c29f4-rabbit-mab/3724#validation-data>).

DyLight 550-conjugated mouse anti-V5: Manufacturer notes confirm that the DyLight 550-conjugated-Mouse anti V5-Tag, clone SV5-Pk1 recognizes the sequence, IPNPLLGLD, present on the P/V proteins of the paramyxovirus, SV5 (Dunn et al. 1999) and can be used to detect recombinant proteins labeled with this V5-tag (Randall et al. 1993 and Zhao et al. 2005).

Other immunohistochemistry looking at neuron anatomy:

The anti-Bruchpilot antibody (DSHB) is the standard in the Drosophila field as a background stain that labels presynaptic active zones to provide neurophil labeling for analysis of anatomy. This antibody was originally validated for use in Drosophila to label presynaptic active zones using immunohistochemistry and to be specific to Bruchpilot protein (Wagh et al. 2006).

The anti-GFP antibody (Adcam) is the standard antibody used in the field for labeling exogenous expression of Green Fluorescent Protein (GFP) in Drosophila, note that this protein is not endogenously expressed in the Drosophila genome. Manufacturer's datasheet confirm that this anti-GFP antibody has been validated using western blot and immunohistochemistry to have specificity for Green Fluorescent Protein. Manufacturer also confirms the use of this antibody for immunolabeling of GFP in Drosophila across 121 peer-reviewer manuscripts (e.g. Sykes et al. 2005 PMID: 16122730).

Animals and other organisms

Policy information about [studies involving animals](#); [ARRIVE guidelines](#) recommended for reporting animal research

Laboratory animals

Below is a complete description from the methods sections of all transgenic Drosophila strains use in this study included how they were obtained and their citation:

The following Gal4 lines were obtained from the Bloomington Drosophila Stock Center (BDSC) and are described in ref. 40: P{R60D05-Gal4}attP2, P{R60D05-lexA}attP40, P{R19C08-lexA}attP40, P{R12B01-Gal4}attP2, P{R54E12-Gal4}attP2, P{R20A02-Gal4}attP2, P{GawB}EB1 was obtained from the BDSC and is described in Wang et al. 2002
 P{20XUAS-IVS-mCD8::GFP}attP40 was a gift from Barret Pfeiffer and Gerry Rubin and is described in Pfeiffer et al, 2010
 P{13XLexAop2-mCD8::GFP}attP40 was obtained from the BDSC and is described in Pfeiffer et al, 2010 PBac{13xLexAop2-IVS-Syn21-Chrimson::tdT-3.1}VK00005 was a gift from Barret Pfeiffer and David Anderson and is described in Hooper et al. 2013
 P{20X-UAS-CsChrimson-tdTomato}VK00005 was a gift from John Tuthill who obtained it from Barret Pfeiffer. P{UAS-Hsap\KCNJ2-EGFP}7 was obtained from the BDSC and is described in Hardie et al. 2001 P{UAS-GCamp6f}attP40 was obtained from the BDSC via Thomas Clandinin and is described in Chen et al. 2013
 Transgenes for MultiColor FlpOut were obtained from the BDSC and are described in Nern et al. 2015 these are w[1118] P{y[+t7.7] w[+mC]=GMR57C10-FLPG5.PEST}su(Hw)attP8; PBac{y[+mDint2]}, and w[+mC]=10xUAS(FRT.stop)myr::smGdP-HA]VK00005 P{y[+t7.7]}, and w[+mC]=10xUAS(FRT.stop)myr::smGdP-V5-THS-10xUAS(FRT.stop)myr::smGdP-FLAG}su(Hw)attP1.

Wild animals

No wild animals were used in this study.

Field-collected samples

No field samples were collected for this study.

Ethics oversight

No ethical approval was required because all experiments in this study were performed on *Drosophila melanogaster*.

Note that full information on the approval of the study protocol must also be provided in the manuscript.